Astronomy & Astrophysics manuscript no. bmontesinos
May 20, 2016

Incidence of debris discs around FGK stars in the solar neighbourhood *

B. Montesinos[1, 3], C. Eiroa[2, 3], A. V. Krivov[4], J. P. Marshall[5, 6], G. L. Pilbratt[7], R. Liseau[8], A. Mora[9], J. Maldonado[10], S. Wolf[11], S. Ertel[12], A. Bayo[13, 14], J.-C. Augereau[15, 16], A. M. Heras[7], M. Fridlund[8, 17], W. C. Danchi[18], E. Solano[1, 19], F. Kirchschlager[11], C. del Burgo[20], and D. Montes[21]

(Affiliations can be found after the references)

Received , ; Accepted

ABSTRACT

Context. Debris discs are a consequence of the planet formation process and constitute the fingerprints of planetesimal systems. Their solar system's counterparts are the asteroid and Edgeworth-Kuiper belts.
Aims. The aim of this paper is to provide robust numbers for the incidence of debris discs around FGK stars in the solar neighbourhood.
Methods. The full sample of 177 FGK stars with $d \leq 20$ pc proposed for the DUNES survey is presented. *Herschel*/PACS observations at 100 and 160 μm complemented in some cases with data at 70 μm, and at 250, 350 and 500 μm SPIRE photometry, were obtained. The 123 objects observed by the DUNES collaboration were presented in a previous paper. The remaining 54 stars, shared with the DEBRIS consortium and observed by them, and the combined full sample are studied in this paper. The incidence of debris discs per spectral type is analysed and put into context together with other parameters of the sample, like metallicity, rotation and activity, and age.
Results. The subsample of 105 stars with $d \leq 15$ pc containing 23 F, 33 G and 49 K stars, is complete for F stars, almost complete for G stars and contains a substantial number of K stars to draw solid conclusions on objects of this spectral type. The incidence rates of debris discs per spectral type are $0.26^{+0.21}_{-0.14}$ (6 objects with excesses out of 23 F stars), $0.21^{+0.17}_{-0.11}$ (7 out of 33 G stars) and $0.20^{+0.14}_{-0.09}$ (10 out of 49 K stars), the fraction for all three spectral types together being $0.22^{+0.08}_{-0.07}$ (23 out of 105 stars). The uncertainties correspond to a 95% confidence level. The medians of the upper limits of $L_{\rm dust}/L_*$ for each spectral type are 7.8×10^{-7} (F), 1.4×10^{-6} (G) and 2.2×10^{-6} (K); the lowest values being around 4.0×10^{-7}. The incidence of debris discs is similar for active (young) and inactive (old) stars. The fractional luminosity tends to drop with increasing age, as expected from collisional erosion of the debris belts.

Key words. stars: circumstellar matter – stars: planetary systems – infrared: stars

1. Introduction

Star and planet formation are linked by the presence of a circumstellar disc built via angular momentum conservation of the original molecular cloud undergoing gravitational collapse (e.g. Armitage 2015). These primordial discs, formed by gas and small dust particles, evolve with the star during the pre-main sequence (PMS) phase and, as they experience gas dispersal and grain growth, are transformed from gas-dominated protoplanetary discs to tenuous, gas-poor, dusty discs, so-called "debris discs". These discs consist of μm-sized particles with short lifetimes, thus, they need to be constantly replenished. Hence, they are second-generation discs, considered to be produced by the constant attrition –due to collisional cascades– of a population of planetesimals (e.g. Wyatt 2008, Krivov 2010).

Primordial discs around young stars, as the birth-sites of planets, provide the initial conditions for planet formation, the raw material and the system's architecture. Some of these young discs have built the ∼2000 exo-solar planets –at the time of writing this paper– distributed in several hundreds of multiple planetary systems that have been found in the last 20 years, mostly around main-sequence (MS) stars[1]. The observed planetary systems as a whole, planets and/or debris discs, present a large variety of architectures (e.g. Marshall et al. 2014, Moro-Martín et al. 2015, Wittenmyer & Marshall 2015), that in conjunction with the host stars, determine the fate of the systems once the stars abandon the MS phase towards later phases of stellar evolution (e.g. Mustill et al. 2014).

A large effort has been devoted to the field of debris discs, with fundamental contributions from space astronomy in the mid- and far-infrared ($\lambda \gtrsim 10$ μm) since the pioneering discovery of an infrared excess in the spectral energy distribution (SED) of Vega provided by the *InfraRed Astronomical Satellite* (IRAS) (Aumann et al. 1984). An enormous amount of references could be provided to cover the vast area of debris discs, their properties, morphology and relationship with the presence of planets. Concerning the topics addressed in this paper, the *Infrared Space Observatory* (ISO, 1995–1998) enlarged the sample of stars observed, studying for the first time the incidence rate of debris discs around MS AFGK stars (Habing et al. 2001) and the time dependency of Vega-like excesses (Decin et al. 2003). The *Spitzer* observatory (cryogenic mission 2003–2009) provided qualitatively and quantitatively large leaps forward, showing that ∼ 16 % of solar-type FGK stars have dusty discs (Trilling et al.

Send offprint requests to: B. Montesinos
e-mail: benjamin.montesinos@cab.inta-csic.es

* *Herschel* is an ESA space observatory with science instruments provided by European-led Principal Investigator consortia and with important participation from NASA.

[1] See http://exoplanetarchive.ipac.caltech.edu/ for updated numbers of exoplanets and multi-planet systems.

2008). The sensitivity of these three missions to debris disc detection was limited by their aperture sizes.

The ESA *Herschel* space observatory (2009–2013) (Pilbratt et al. 2010), with its 3.5-m aperture, and imaging photometers PACS (Poglitsch et al. 2010), and SPIRE (Griffin et al. 2010), providing an increased sensitivity to debris discs (see Fig. 1 in Eiroa et al. 2013), a wider wavelength coverage, and ability to spatially resolve many of them, has been fundamental in extending the picture. An account of results of the pre-*Herschel* era can be found in the review by Wyatt (2008), whereas a much more comprehensive view, including some of the *Herschel* results is given by Matthews et al. (2014).

Eiroa et al. (2013) (E13 herafter), presented the results obtained from the *Herschel* Open Time Key Programme (OTKP) DUNES[2,3], DUst around NEarby Stars. This programme aimed to detect Edgeworth-Kuiper belt (EKB) analogues around nearby solar-type stars. The incidence rate of debris discs in a $d \leq 20$ pc subsample was 20 ± 2 %. However, the sample of FGK stars observed and analysed in that paper was not complete (see Section 2.2 for details), therefore it is mandatory to analyse data on a complete –or near-complete– sample, in order to avoid biased conclusions.

This paper analyses the full sample of solar-type (FGK) stars of the DUNES programme located at $d \leq 20$ pc, as it was described in the original DUNES proposal, i.e. the subsample studied in E13 plus the stars shared with, and observed within, the OTKP DEBRIS, Disc Emission via a Bias-free Reconnaissance in IR and Sub-mm (Matthews et al. 2010). The scientific background, context and rationale of the present work are the same as those presented in E13; they were described in detail in Sections 1 and 2 of that paper and therefore the information will not be duplicated again here. Special attention is paid to the DUNES subsample of stars with $d \leq 15$ pc, which is complete for F stars, almost complete for G stars, and has a substantial number of K stars, making the conclusions, concerning the incidence rate of debris discs in the corner of our Galaxy, fairly robust.

The paper is organized as follows. In Sect. 2, the sample of stars is described; the reasons why the observations of the full DUNES sample were split between the DUNES and DEBRIS teams are explained; the completeness of the sample is discussed, and comprehensive information on the optical and near-IR photometry of the shared sample used to build the spectral energy distributions is also given. In Sect. 3, the observations and data reduction are described. The results are presented in Sect. 4. The analysis of the full DUNES sample is done in Sect. 5 and a summary of the main conclusions is presented in Sect. 6.

2. The stellar sample

2.1. Selection criteria

The stellar sample analysed in this work is the merger of the sample studied in E13, which will be called DUNES_DU in this paper, and a subsample of FGK stars observed by the DEBRIS team, which will be identified here as DUNES_DB. The full DUNES sample is composed of the merger of DUNES_DU and DUNES_DB. We will concentrate our analysis on the stars with $d \leq 20$ pc and pay special attention, when addressing the incidence rates of debris discs, to the subset within 15 pc. Below, we give details of the DUNES_DU and DUNES_DB subsamples.

DUNES and DEBRIS were two complementary *Herschel* programmes with different observing strategies and different approaches to the selection criteria for their samples. Given the overlapping scientific interests of both projects, the *Herschel* Time Allocation Committee suggested to split the samples in the most convenient and efficient way, keeping the philosophy and observing strategy of the corresponding science cases. Both teams were granted with the same amount of observing time (140 hours).

Table 1. Summary of spectral types in the DUNES_DU and DUNES_DB samples.

Sample	F	G	K	Total
DUNES_DU	27	52	54	133
≤ 15 pc DUNES_DU subsample	4	19	43	66
≤ 20 pc DUNES_DU subsample	19	50	54	123
DUNES_DB	51	24	6	81
≤ 15 pc DUNES_DB subsample	19	14	6	39
≤ 20 pc DUNES_DB subsample	32	16	6	54

Note on the nomenclature of the samples:

DUNES_DU contains the stars of the DUNES sample observed by the DUNES team, DUNES_DB contains the stars of the DUNES sample observed by the DEBRIS team.

As described in E13, the original DUNES stellar sample, out of which the final sample was built, was chosen from the *Hipparcos* catalogue (VizieR online catalogue I/239/hip_main, Perryman et al. 1997) following the only criterion of selecting MS –luminosity class V-IV/V– stars closer than 25 pc, without any bias concerning any property of the objects. The restriction to build the final sample was that the stellar photospheric emission could be detected by PACS at 100 μm with a S/N≥5, i.e., the expected 100 μm photospheric flux should be significantly higher than the expected background as estimated by the Herschel HSPOT tool at that wavelength. Two stars, namely τ Cet (HIP 8102, G8 V) and ϵ Eri (HIP 16537, K2 V), although fulfilling all the selection criteria described above, do not belong to the DUNES sample because they were included in the Guaranteed Time Key Programme "Stellar Disk Evolution" (PI: G. Olofsson).

Taking into account the amount of observing time allocated and the complementarity with DEBRIS, the sample observed by the DUNES team was restricted to main-sequence FGK solar-type stars located at distances shorter than 20 pc. In addition, FGK stars between 20 and 25 pc hosting exoplanets (3 stars, 1 F-type and 2 G-type, at the time of the proposal writing) and previously known debris discs, mainly from the *Spitzer* space telescope (6 stars, all F-type) were also included. Thus, the sample of stars directly observed by DUNES, which we call DUNES_DU in this paper[4], is composed of 133 stars, 27 out of which are F-type, 52 G-type, and 54 K-type stars. The 20 pc subsample was formed by 123 stars –19 F-type, 50 G-type and 54 K-type[5].

[2] http://www.mpia-hd.mpg.de/DUNES/

[3] http://sdc.cab.inta-csic.es/dunes/

[4] Note that this subsample was formally called the "DUNES sample" in E13, but it is actually only the subset of the full DUNES sample that was observed within the DUNES observing time.

[5] In E13, the sample of stars within 20 pc was composed of 124 objects because the selection of the initial sample was done according to the original ESA 1997 release of the *Hipparcos* catalogue; in that release the parallax of HIP 36439 was 50.25 ± 0.81 mas. However, in

The OTKP DEBRIS was defined as a volume limited study of A through M stars selected from the "UNS" survey (Phillips et al. 2010), observing each star to a uniform depth, i.e., DEBRIS was a flux-limited survey. In order to optimize the results according to the DUNES and DEBRIS scientific goals, the complementarity of both surveys was achieved by dividing the common stars of both original samples, considering whether the stellar photosphere could be detected with the DEBRIS uniform integration time. Those stars were assigned to be observed by DEBRIS. In that way, the DUNES observational requirement of detecting the stellar photosphere was satisfied. The few common A- and M-type stars in both surveys were also assigned to DEBRIS.

The net result of this exercise was that 106 stars observed by DEBRIS satisfy the DUNES photospheric detection condition and are, therefore, shared targets. Specifically, this sample comprises 83 FGK stars –51 F-type, 24 G-type and 8 K-type (the remaining stars are of spectral type A and M). Note that spectral types listed in the *Hipparcos* catalogue are used to give these numbers, we will see below that two K stars had to be excluded due to a wrong spectral type classification. Since the assignment to one of the teams was made on the basis of both DUNES and DEBRIS original samples, the number of shared targets located closer than 20 pc, i.e., the revised DUNES distance, is fewer: 56 FGK - 32 F-type, 16 G-type, and 8 K-type stars.

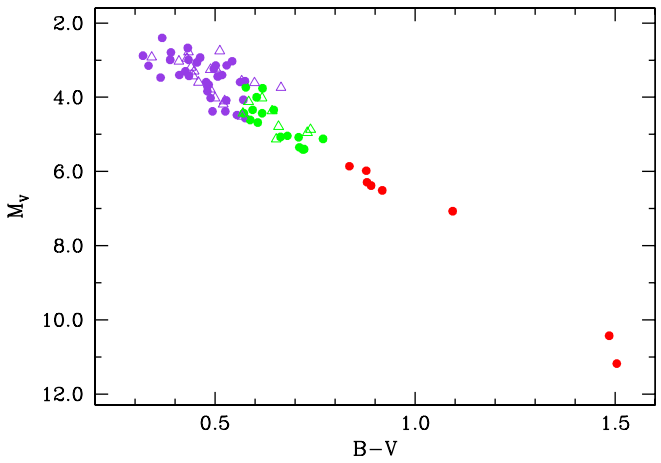

Fig. 1. HR diagram for the FGK stars of the DUNES sample observed by the DEBRIS team (DUNES_DB). Colour codes -following the *Hipparcos* spectral types are: F stars (violet), G stars (green), K stars (red). Solid circles represent FGK stars closer than 20 pc; empty triangles are FGK stars further away. The two red dots at the bottom right of the diagram are two stars classified as K5 in the *Hipparcos* catalogue but their colours correspond to M stars. See text for details.

In Fig. 1 we show the HR diagram M_V–(B–V) for the sample of FGK stars of the DUNES sample observed during the DEBRIS observing time. Solid circles represent FGK stars closer than 20 pc –i.e. the subsample analysed in this paper– whereas empty triangles have been used to plot FGK stars further away, not included in the study presented here. Two stars, namely HIP 84140 and HIP 91768 –the two red dots at the bottom right of the diagram– both are classified as K5 in the *Hipparcos* catalogue, but their (B–V) colours clearly correspond to that of an ∼M3 star (the spectral type listed in SIMBAD for both objects), therefore they have been moved out of the FGK star sample. We identify the subsample of 81 FGK stars as DUNES_DB in this paper, out of which 54 are closer than 20 pc. Table 1 summarizes the spectral type distribution of the DUNES_DU and DUNES_DB samples, taking into account these two misclassifications.

Table 2 provides some basic information of the FGK stars within $d \leq 20$ pc of the DUNES_DB sample[6] (the corresponding information for the DUNES_DU sample can be found in Table 2 of E13). Columns 1, 2 and 3 give the *Hipparcos*, and HD numbers, and an alternative denomination. *Hipparcos* spectral types are given in column 4. In order to check the consistency of these spectral types we have explored VizieR using the DUNES discovery tool[7] (see Appendix A in E13). Results of this exploration are summarized in column 5 which gives the spectral type range of each star taken into account SIMBAD, Gray et al. (2003, 2006), Wright et al. (2003) and the compilation made by Skiff (2009). The typical spectral type range is 2-3 subtypes. Columns 6 and 7 list the equatorial coordinates and columns 8 and 9 give parallaxes with errors and distances, respectively. The parallaxes are taken from van Leeuwen (2007) (VizieR online catalogue I/311). Parallax errors are typically less than 1 mas. Only one star, namely HIP 46509, has an error larger than 2 mas, this object being a spectroscopic binary (see Table 4). The multiplicity status of the DUNES_DB sample is addressed in Sect. 2.4.

2.2. Completeness

The main constraint affecting the completeness of the sample is the observational restriction that the photosphere had to be detected with a S/N≥5 at 100 μm. It is important to know the impact of this restriction in order to assess the robustness of the results concerning the frequency of the incidence of debris discs in the solar neighbourhood.

In Fig. 2 the cumulative numbers of stars in the merged DUNES_DU and DUNES_DB $d \leq 15$-pc and $d \leq 20$-pc samples –normalized to the total number of objects in each one– have been plotted against stellar mass as red and blue histograms, respectively. The masses have been assigned to each star by linear interpolation of the values given for FGK MS stars by Pecaut & Mamajek (2013)[8] using (B–V) as the independent variable. The expected mass spectrum for the solar neighbourhood according to a Salpeter law (Salpeter 1955) with exponent −2.35 has been normalized to the total cumulative number of each sample and plotted in green. It is clear that the sample with $d \leq 20$ pc shows an underabundace of stars below ∼1.2 $M_\odot$ whereas the behaviour of the sample with $d \leq 15$ pc approximates that of the Salpeter law, but still runs slighly below at low masses. Similar results are obtained using other approaches for the mass spectrum, e.g. that by Kroupa (2001). In grey, the cumulative distribution for the FGK stars with $d \leq 15$ pc from the *Hipparcos* catalogue has been also included, showing a much closer agreement with the Salpeter law.

Since the DUNES sample was drawn from the *Hipparcos* catalogue, it is important to assess the problem of its completeness. In Sect. 2.2 of Turon et al. (1992) it can be seen that the *Hipparcos* Input Catalogue was only complete down to $V = 7.3$

the revision by van Leeuwen (2007) the parallax is 49.41 ± 0.36 mas, putting this object beyond 20 pc. Here we exclude this star from the DUNES_DU 20-pc sample, and consider only 123 stars in that subset.

[6] Excerpts of Tables 2, 3, 5 and 7 are included in the main body of the manuscript. The full tables can be found at the end of the paper and are available in electronic format.

[7] http://sdc.cab.inta-csic.es/dunes/searchform.jsp

[8] See also "Stellar Color/Teff Table" under section "Stars" in http://www.pas.rochester.edu/∼emamajek/

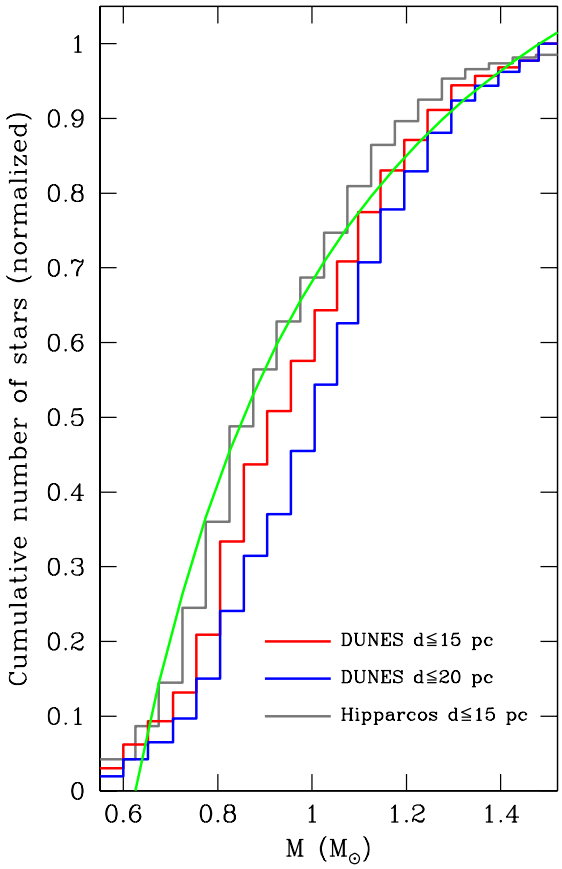

Fig. 2. Cumulative distributions (normalized) for the DUNES samples with $d \leq 15$ pc (105 stars, red) and $d \leq 20$ pc (177 stars, blue) and the FGK stars in the *Hipparcos* catalogue with $d \leq 15$ pc (154 stars, grey), all plotted against stellar mass. A Salpeter law with exponent −2.35 has been normalized to the distributions. See text for details.

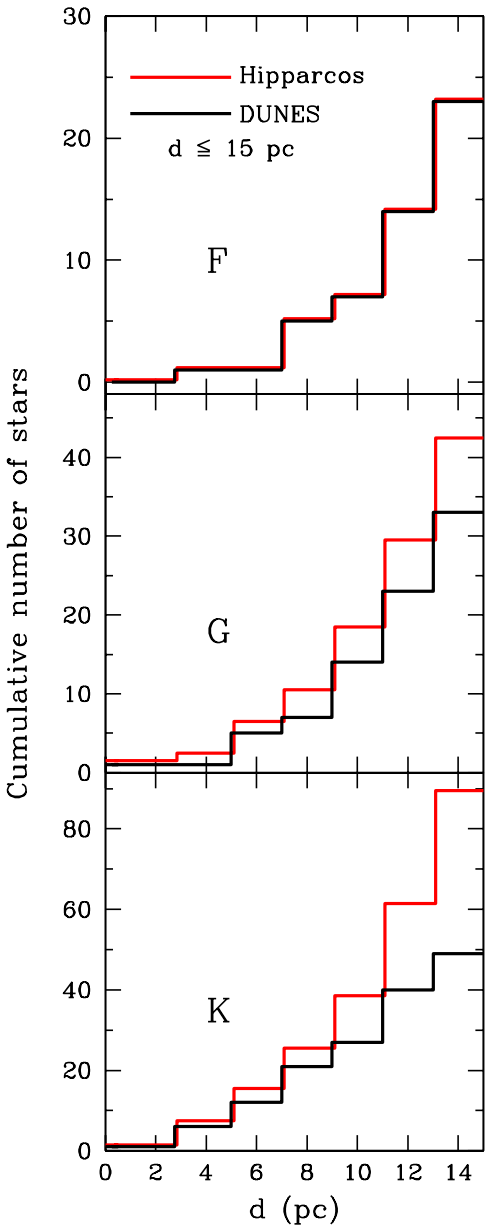

Fig. 3. Cumulative number of F, G and K stars (luminosity classes V and IV-I) in the *Hipparcos* catalogue (red) and in the DUNES sample (black), both at $d \leq 15$ pc.

for stars cooler than G5. For $d = 15$ pc, this corresponds to an spectral type of ∼K2. In addition, not all the stars in the Input Catalogue were observed (see Table 1 of Turon et al. 1992): for the magnitude bin $V : 7-8$ the efficiency of the survey was 93%, therefore, even applying a safety margin of 0.3 mag, we would have completeness only up to spectral type K1. In summary, down to 15 pc, *Hipparcos* is complete for F and G but not for K stars.

To quantify the departure of the full DUNES $d \leq 15$-pc sample from the parent *Hipparcos* set, we have compared the number of stars of each spectral type in our sample with the corresponding numbers in the *Hipparcos* catalogue. In Fig. 3, cumulative histograms of the numbers of F, G, and K stars (luminosity classes V and IV-V) in the *Hipparcos* catalogue (red), and in the DUNES sample (black), both at $d \leq 15$, are plotted against distance. The total numbers of stars are 23 F, 42 G, 89 K in *Hipparcos* against 23 F, 33 G, 49 K in the DUNES sample, i.e., the observational constraint imposed in the final selection of the targets keeps all the F stars from *Hipparcos* but discards 9 G and 40 K stars. Therefore, a correction on the fraction of excesses extracted from the DUNES sample would have to be applied –in particular for K stars– in order to give results referred to a wider sample. We will come back to this point in Sect. 4.

2.3. Stellar parameters of the DUNES_DB sample

Table 3 gives some parameters of the DUNES_DB objects with $d < 20$ pc, namely the effective temperature, gravity, and metallicity (cols. 2–4, and a flag in col. 5 indicating whether the determination was spectroscopic or photometric), the stellar luminosity (col. 6) and the activity indicator $\log R'_{\rm HK}$ (col. 7 and its correspondent reference in col. 8). References for $T_{\rm eff}$, $\log g$, [Fe/H] and $\log R'_{\rm HK}$ are given at the bottom of the table. The luminosity was computed using equation (9) from Torres (2010), with the values of the V-magnitude and colour index $(B-V)$ taken from the *Hipparcos* catalogue, and the bolometric corrections (BC) from Flower (1996); $(B-V)$ was used as the independent variable to obtain BC.

Col. 9 lists the rotation periods, $P_{\rm rot}$, estimated using the strong correlation between $\log R'_{\rm HK}$ and the Rossby number, de-

Table 2. The subsamples of DUNES_DB with $d \leq 15$ pc and $15\,\mathrm{pc} < d \leq 20$ pc (only the first stars are shown).

HIP	HD	Other ID	SpT (Hipparcos)	SpT range	ICRS (2000)		π(mas)	d(pc)
FGK stars ($d \leq 15$ pc)								
1599	1581	ζ Tuc	F9V	F9.5V, F9V–G0V	00 20 04.260	−64 52 29.25	116.46±0.16	8.59±0.01
3765	4628	LHS 121	K2V	K2.5V, K2V	00 48 22.977	+05 16 50.21	134.14±0.51	7.45±0.03
7751	10360J	p Eri	K0V	K0V, K1–K3V	01 39 47.540	−56 11 47.10	127.84±2.19	7.82±0.13
...								
FGK stars ($15\,\mathrm{pc} < d \leq 20$ pc)								
5862	7570	ν Phe	F8V	F9V, F9V	01 15 11.121	−45 31 54.00	66.16±0.24	15.11±0.05
17651	23754	27 Eri	F3/F5V	F5IV-V, F3III	03 46 50.888	−23 14 59.00	56.73±0.19	17.63±0.06
36366	58946	ρ Gem	F0V...	F0V, F0V–F3V	07 29 06.719	+31 47 04.38	55.41±0.24	18.05±0.08
...								

fined as $\mathrm{Ro} = P_{\mathrm{rot}}/\tau_{\mathrm{c}}$, where τ_{c} is the convective turnover time, which is a function of the spectral type (colour) (Noyes et al. 1984, Montesinos et al. 2001, Mamajek & Hillenbrand 2008). For six objects, the estimation of P_{rot} was not feasible due to the fact that the calibrations do not hold for the values of either $\log R'_{\mathrm{HK}}$ or $B-V$; in that case, lower limits of the rotation period, based on the values of $v \sin i$, are given. Cols. 10 and 11 show the stellar ages t_{Gyro} and t_{HK} computed according to gyrochronology and using the chromospheric emission as a proxy for the age. In Appendix A we give details of the estimation of the rotation periods and ages.

2.4. Multiplicity

Table 4 lists the multiplicity properties of the objects that are known to be binaries. The importance of this information cannot be underestimated, specially when the spectral types of the components are close –and hence ΔV is small– and the binary is spectroscopic or its components have not been resolved individually during a particular spectroscopic or photometric observation from which a given parameter is derived. In many cases parameters are assigned as representative of the whole system, without reference in the literature to which component they refer to. This has also an impact on the calculation of the corresponding model photospheres that are used, after normalization to the optical and near-IR photometry, as baselines to detect potential excesses at the *Herschel* wavelengths. Concerning the data given in Table 4, this has to be taken into account for HIP 7751 ($\Delta V = 0.16$), HIP 44248 (1.83), HIP 61941 (0.04), HIP 64241 (0.68), HIP 72659 (2.19), HIP 73695 (0.87), and HIP 75312 (0.37), as well as for those stars classified as "spectroscopic binaries" for which no information on their components is available. The proper motions of the components have been extracted from the "*Hipparcos* and *Tycho* catalogues (Double and Multiples: Component solutions)" (VizieR online catalogue I/239/h_dm_com).

The bottom part of Table 4 gives information about the stars of the DUNES_DB sample with $d \leq 20$ pc that, at the time of writing this paper, have confirmed exoplanets. The mass and the length of the semimajor axis of the orbit for each planet are given.

2.5. Photometry

Tables 5a–5d give the optical, near-IR, AKARI, WISE, IRAS and *Spitzer* MIPS magnitudes and fluxes of the DUNES_DB stars with $d \leq 20$ pc, and the corresponding references. This photometry has been used to build and trace the spectral energy distributions (SEDs) of the stars, that are, along with PHOENIX/Gaia models (Brott & Hauschildt 2005), the tools to predict the fluxes at the far-IR wavelengths in order to determine whether or not the observed fluxes at those wavelengths are indicative of a significant excess. Appendix C in E13 gives details on the photospheric models and the normalization procedure to the observed photometry. In addition to the photometry, *Spitzer*/IRS spectra of the targets, built by members of the DUNES consortium from original data from the *Spitzer* archive, are included in the SEDs, although they have not been used in the process of normalization of the photospheric models.

3. *Herschel* observations of the DUNES_DB sources and data reduction

3.1. PACS observations

As described by Matthews et al. (2010), DEBRIS is a flux-limited survey where each target was observed to a uniform depth (1.2 mJy beam^{-1} at 100 μm). The observations of the DUNES_DB sources were performed by the DEBRIS team with the ESA *Herschel* Space Observatory using the instrument PACS. Further details can be found in the paper by Matthews et al. (2010). The main parameters of the observational set up used by DEBRIS are compatible with those used by DUNES and described in E13.

3.2. Data reduction

Data for each source comprise a pair of mini scan-map observations taken with the PACS 100/160 waveband combination. DEBRIS and DUNES observations both followed the same pattern for mini scan-map observations (see PACS Observer's Manual, Chapter 5), with minor differences in the scan leg lengths (8′ for DEBRIS, 10′ for DUNES) leading to slightly different coverage across the resulting map areas for the two surveys, in addition to the different map depths. These differences are immaterial to the analysis presented here. The *Herschel* PACS observations were reduced in the Herschel Interactive Processing Environment (Ott 2010). For the analysis presented here we used HIPE version 10 and PACS calibration version 45. Reduction was carried out following the same scheme as presented in E13. Table 6 shows a log of the observations with details of the OBSIDs and the on-source integration times.

The individual PACS scans of each target were high-pass filtered to remove large-scale background structure, using high pass filter radii of 20 frames at 100 μm and 25 frames at 160 μm, suppressing structures larger than 82″ and 102″ in the final images, respectively. For the filtering process, a region 30″ radius around the source position in the map along with regions where the pixel brightness exceeded a threshold defined as twice the

Table 3. Parameters of the DUNES_DB stars with $d \leq 15$ pc and 15 pc $< d \leq 20$ pc (only the fist stars are shown).

HIP	$T_{\rm eff}$ (K)	$\log g$ (cm/s^2)	[Fe/H] (dex)	Flag	$L_{\rm bol}$ ($L_\odot$)	$\log R'_{\rm HK}$	Ref	$P_{\rm rot}$ (d) or lower limit†	$t_{\rm Gyro)}$ (Gyr)	$t_{\rm HK}$ (Gyr)
FGK stars ($d \leq 15$ pc)										
1599	5960	4.45	−0.17	S	1.224	−4.855	1	14.01 ± 0.97	2.20	4.03
3765	4977	4.57	−0.22	S	0.283	−4.852	2	39.02 ± 0.25	5.41	3.98
7751	4993	4.54	−0.23	S	0.304	−4.94	3			
7918	5891	4.36	+0.06	S	1.405	−4.987	4	21.10 ± 0.12	3.56	6.36
7981	5189	4.52	−0.04	S	0.439	−4.912	2	39.60 ± 0.43	6.04	4.99

Table 5a. Johnson V, $B-V$, Cousins $V-I$ and Strömgren photometry.

HIP	V (mag)	$B-V$ (mag)	$V-I$ (mag)	$b-y$ (mag)	m_1 (mag)	c_1 (mag)
FGK stars ($d \leq 15$ pc)						
1599	4.23	0.576±0.010	0.65±0.02	0.368±0.003	0.177±0.004	0.302±0.020
3765	5.74	0.890±0.008	0.97±0.02	0.512±0.003	0.423±0.002	0.255±0.004
7751	5.76	0.880±0.400	0.93±0.02	0.512	0.421	0.262
7918	4.96	0.618±0.001	0.67±0.03	0.389±0.000	0.198±0.005	0.348±0.011
7981	5.24	0.836±0.008	0.88±0.01	0.492±0.002	0.367±0.007	0.296±0.006

Table 5b. 2MASS $JHK_{\rm s}$ and ancillary Johnson $JHKLL'M$ photometry.

HIP	2MASS J (mag)	2MASS H (mag)	2MASS $K_{\rm s}$ (mag)	Qflag	J (mag)	H (mag)	K (mag)	L (mag)	L' (mag)	M (mag)	Refs.
FGK stars ($d \leq 15$)											
1599	3.068±0.272	2.738±0.218	2.769±0.250	DDD	3.196	2.880	2.832	2.803	2.795	2.856	1,2,3
3765	4.367±0.310	3.722±0.230	3.683±0.268	DDD							
7751A			3.558±0.270	D							
7751B	4.043±0.378		3.510±0.282	D D							
7918	4.000±0.262	3.703±0.226	3.577±0.314	DDD	3.800	3.560					2
7981	3.855±0.240	3.391±0.226	3.285±0.266	DDD	3.775	3.345	3.285				2

Table 5c. AKARI 9 and 18 μm fluxes and WISE W1, W3 and W4 photometry.

HIP	AKARI		WISE		
	9 μm (mJy)	18 μm (mJy)	3.35 μm (W1) (mag)	11.56 μm (W3) (mag)	22.09 μm (W4) (mag)
FGK stars ($d \leq 15$ pc)					
1599	4191±28	1055±30		2.856±0.011	2.788±0.019
3765	2199±15	519±8		3.370±0.039	3.493±0.023
7751	3431±198	892±20			3.095±0.053
7751B	1810±135				
7918	2280±24	494±12	3.489±0.423	3.469±0.012	3.444±0.018
7981	2724±5.	586±39	3.274±0.479		3.312±0.033

Table 5d. IRAS 12, 25, 60 μm and *Spitzer*/MIPS 24 and 70 μm fluxes.

HIP	IRAS						MIPS	
	12 μm (mJy)	%	25 μm (mJy)	%	60 μm (mJy)	%	24 μm (mJy)	70 μm (mJy)
FGK stars ($d \leq 15$ pc)								
1599	3.11×10^3	4	6.95×10^2	4			519±11	82±8
3765	1.56×10^3	7					264±5	26±10
7751	2.70×10^3	5	6.55×10^2	7			231±4	22±4
7918	1.67×10^3	5	3.87×10^2	8			289±6	25±11
7981	1.87×10^3	7	6.38×10^2	10			334±7	48±9

standard deviation of the non-zero flux elements in the map (determined from the level 2 pipeline reduced product) were masked from inclusion in the high pass filter calculation. Regions external to the central 30″ that exceeded the threshold were tagged as source to be avoided in the background estimation phase of the flux extraction process. Deglitching was carried out using the spatial deglitching task in median mode and a threshold of 10-σ. For the image reconstruction, a drop size (`pixfrac` parameter) of 1.0 was used. Once reduced, the two individual PACS scans in each waveband were mosaicked to reduce sky noise and suppress $1/f$ striping effects from the scanning. Final image scales were 1″ per pixel at 100 μm and 2″ per pixel at 160 μm, compared to native instrument pixel sizes of 3.2″ for 100 μm, and 6.4″ for 160 μm.

4. Results

The extraction of PACS photometry of the sources analysed in this paper follows identical procedures as those in E13. Sect. 6.1.1 of that paper contains a very detailed description of the procedures to carry out the flux extraction. Summarizing, flux densities were measured using aperture photometry. If the image was consistent with a point source, then an aperture appropriate to maximise the signal-to-noise was adopted (i.e. 5″ at 100 μm, and 8″ at 160 μm, see E13). Regarding extended sources, we refer the reader to Sect. 7.2.3 of E13, where the criteria to assess whether the 3σ flux contours in the 100 and 160 μm images denote extended emission are described.

The background and rms scatter were estimated from the mean and standard deviation of 10 square sky apertures placed at random around the image. The sky apertures were sized to have roughly the same area as the source aperture. The locations of the sky apertures were chosen such that they did not overlap with the source aperture or any background sources (to avoid contamination), and lay within 60″ of the source position (to avoid higher noise regions at the the edges of the image).

Measured flux densities in each PACS waveband were corrected for the finite aperture size using the tabulated encircled energy fractions given in Balog et al. (2014), but have not been colour corrected[9]. A point-source calibration uncertainty of 5% was assumed for all three PACS bands. Note that aperture corrections valid for point sources have been also applied to the case of extended sources. This is obviously an approach, but it should be valid as long as the aperture size is larger than the extended source. This criterion has widely been used, without any apparent inconsistency, in other works, e.g. Wyatt et al. (2012) for 61 Vir, Duchêne et al. (2014) for η Crv, Roberge et al. (2013) for 49 Cet.

Table 7 lists the PACS 100 and 160 μm photometry and 1σ uncertainties for the sources of the DUNES_DB sample with $d \leq 20$ pc, identified as the far-IR counterparts of the optical stars. Uncertainties include both the statistical and systematic errors added in quadrature; the uncertainty in the calibration is 5% in both bands (Balog et al. 2014). Quantities without errors in the PACS160 column correspond to 3σ upper limits. In the columns adjacent to the PACS photometry, the photospheric predictions, $S_\nu(\lambda)$, with the corresponding uncertainties, are given. The fluxes $S_\nu(\lambda)$ are extracted from a Rayleigh-Jeans extrapolation of the fluxes at 40 μm from the PHOENIX/Gaia normalized models. The uncertainties in the individual photospheric fluxes were estimated by computing the total σ of the normalization, in logarithmic units; in that calculation, the observed flux at each wavelength involved in the normalization process was compared with its corresponding predicted flux. The normalized model $\log S_\nu(\lambda)$ was permitted to move up and down a quantity $\pm\sigma$. That value of σ was then translated into individual –linear– uncertainties of the fluxes, $\sigma(S_\nu(\lambda))$, at the relevant *Herschel* wavelengths. The typical uncertainty in the photospheric predictions derived from a change of ±50 K in $T_{\rm eff}$ for a model with 6000 K amounts ∼0.9% of the predicted flux density. It has not noticeable effects in any of the calculations.

We consider that an object has an infrared excess at any of the PACS wavelengths when the significance:

$$\chi_\lambda = \frac{\mathrm{PACS}_\nu(\lambda) - S_\nu(\lambda)}{(\sigma(\mathrm{PACS}_\nu(\lambda))^2 + \sigma(S_\nu(\lambda))^2)^{1/2}} > 3.0 \quad (1)$$

although in some cases the complexity of the fields makes it difficult to ascertain whether an apparent clear excess based solely on the value of χ_λ is real or not.

The values of χ_{100} and χ_{160} are listed in Table 7 along with the status "Excess/No excess" or "Dubious" in the last column, derived both from those numbers and a careful inspection of the fields.

In addition, PACS 70 μm and SPIRE photometry from the literature were included for HIP 61174, HIP 64924 and HIP 88745, and PACS 70 μm photometry for HIP 15510. The fluxes and the corresponding references are given at the bottom of Table 7.

4.1. Stars with excesses

After a careful analysis of the corresponding images and surrounding fields, 11 stars of the DUNES_DB sample with $d \leq 20$ pc are considered as showing real excesses among those in Table 7 having χ_{100} and/or $\chi_{160} > 3.0$. They are listed in the upper half of Table 8.

Eight sources show excess at both 100 and 160 μm; these are HIP 15510, HIP 16852, HIP 57757, HIP 61174, HIP 64924, HIP 71284, HIP 88745 and HIP 116771.

Two sources, HIP 5862 and HIP 23693, show excess only at 100 μm and fluxes at 160 μm slightly above the photospheric flux but not large enough to give $\chi_{160} > 3.0$. Consequently they present a decrease in their SED for $\lambda \geq 100$ μm, similar to those in three stars in DUNES_DU (HIP 103389, HIP 107350 and HIP 114948). An extensive modelling of these three objects was done by Ertel et al. (2012) and their conclusions can be applied to HIP 5862 and HIP 23693.

HIP 113283 shows excess only at 160 μm, therefore it is a cold-disc candidate as those discovered and modelled by Eiroa et al. (2011), E13, Krivov et al. (2013) and Marshall et al. (2013).

Among the 11 sources with confirmed excesses, five have been spatially resolved. They are marked with an asterisk in Tables 7 and 8. Four of them were already known, namely HIP 15510 (Wyatt et al. 2012, Kennedy et al. 2015), HIP 61174 (Matthews et al. 2010,Duchêne et al. 2014), HIP 64924 (Wyatt et al. 2012) and HIP 88745 (Kennedy et al. 2012).

The fifth extended source found in this work is HIP 16852. A 2-dimensional Gaussian fit gives full-widths at half-maximum (FWHM) along the principal axes of 7.7″×8.5″at 100 μm, and 12.2″×10.5″at 160 μm, where those of the PSF along the same directions at each wavelength are 6.9″×6.8″and 11.8″×10.9″, respectively. This implies that the source is marginally resolved at 100 μm. Thus, HIP 16852 is similar in terms of angular size

[9] See PACS Technical Notes PICC-ME-TN-038 and PICC-ME-TN-044.

Table 7. PACS flux densities for the DUNES_DB stars with $d \leq 15$ pc and 15 pc $< d \leq 20$ pc (only the first stars are shown).

HIP	HD	PACS100 (mJy)	S100 (mJy)	χ_{100}	PACS160 (mJy)	S160 (mJy)	χ_{160}	Status
FGK stars ($d \leq 15$ pc)								
1599	1581	33.23± 2.35	30.08± 0.19	1.34	29.03±3.46	11.75± 0.07	4.99	Dubious
3765	4628	19.43± 1.93	15.84± 0.36	1.83	< 3.38	6.19± 0.14		No excess
7751	10360	11.95± 1.70	12.39± 0.21	−0.26	< 5.00	4.84± 0.08		No excess
	10361	10.66± 1.68	14.90± 0.26	−2.49	< 5.00	5.82± 0.10		No excess
7918	10307	14.33± 1.75	16.21± 0.25	−1.06	10.35±3.17	6.33± 0.10	1.27	No excess
7981	10476	20.18± 1.91	20.05± 0.21	0.07	7.87±2.05	7.83± 0.08	0.02	No excess

to HIP 15510, which was also marginally resolved at 100 μm by Kennedy et al. (2015)[10].

Among the excess sources, planets have been detected around HIP 15510 (Pepe et al. 2011), and HIP 64924 (Vogt et al. 2010), see details in Table 4.

In addition to the excess sources, nine more objects have χ_{100} and/or $\chi_{160} > 3.0$ but are labelled in Table 7 as "Dubious" because of the complexity of the fields that makes an unambiguous measurement of the fluxes difficult. They are listed in the lower half of Table 8. These are HIP 1599, HIP 36366, HIP 44248, HIP 37279, HIP 59199, HIP 61941 (all of them F-type), HIP 72659, HIP 73695 (binaries with a primary of G-type) and HIP 77257 (G).

In Table 8, we give the results for $T_{\rm BB}$, estimated from black body fittings, and the fractional luminosity $L_{\rm dust}/L_*$ computed by integrating directly on one hand the black body curve that best fits the excess, and on the other, the normalized photospheric model. Values are given both for the stars with confirmed and apparent excesses. Typical uncertainties in the black-body temperatures are ±10 K. For all the stars, apart from HIP 61174, the data involved in the black-body fittings are only the PACS –and SPIRE, if available– flux densities. For HIP 61174, the fit to the warm black body includes all the ancillary photometry between 10 and 30 μm (WISE W3 and W4, Akari 18, MIPS 24, IRAS 12 and 25) collected by us and listed in Tables 5c and 5d.

The values of the fractional luminosity that appear in the table for HIP 5862 and HIP 23693 correspond to modified black body fits to all the points showing excess, however, those fits have been used just to integrate the excess fluxes, since the values of β –the parameter modifying the pure black body in $(\lambda_0/\lambda)^\beta$– are unreasonably high in both cases, of the order of ∼6.0, making a physical interpretation very difficult; most probably a two-ring disc would be more adequate to model those two cases. The black body radii computed according to the expression

$$R_{\rm BB} = \left(\frac{278}{T_{\rm BB}({\rm K})}\right)^2 \left(\frac{L_*}{L_\odot}\right)^{1/2} \quad (2)$$

(see e.g. Backman & Paresce 1993) are also included in the table.

Figs. B.1 and B.2 show the SEDs of the sources with confirmed and dubious excesses, respectively. In blue we have plotted all the photometry available below 70 μm, in red the PACS –and SPIRE for some objects– fluxes, in black the model photosphere normalized, and in green the black body fits to the excess.

[10] An inspection of the image at 70 μm from the 70/160 waveband combination, that has not be used in this work, shows that HIP 16852 is also extended at this wavelength.

Information of some of these sources has been already reported in other works. Gáspár et al. (2013) compiled a catalogue of *Spitzer*/MIPS 24 and 70 μm, and *Herschel*/PACS 100 μm observations that includes the stars analysed in this paper. They confirm excesses for seven out of the 11 stars listed at the top of Table 8, the exceptions being HIP 57757 ($\chi_{100} = 1.01$) and HIP 71284 ($\chi_{100} = 3.35$, but no MIPS data available); HIP 113283 is obviously labelled as "no-excess" by these authors because they did not analyse the observation at 160 μm, the wavelength where we detect an excess. For HIP 116771 they do not provide the PACS 100 μm flux and the star is catalogued as a non-excess source according to the MIPS 70 μm ($\chi_{70} = 1.77$).

Chen et al. (2014) analysed and modelled the SEDs of 499 targets that show *Spitzer*/IRS excesses, including a subset of 420 targets with MIPS 70 μm observations. They found that the SEDs for the majority of objects (∼66%) were better described using a two-temperature model with warm ($T_{\rm dust} \sim 100 - 500$ K) and cold ($T_{\rm dust} \sim 50 - 150$ K) dust populations analogous to zodiacal and Kuiper Belt dust. Four of their excess sources for which we also find an excess in the far-IR appear in Chen et al. (2014) (VizieR online catalogue J/ApJS/211/25): HIP 5862, HIP 23693 and HIP 64924 are modelled with two-temperature fits, the cold components having $T_{\rm dust} = 94 \pm 8$, 51 ± 7 and 54 ± 10 K, respectively, whereas HIP 16852 is reproduced by a one-temperature fit with $T_{\rm dust} = 100 \pm 6$ K. The single black-body fits for those stars (see Table 8) are 96, 82, 50 and 87 K, respectively, which do not deviate much from the determinations by Chen et al.

Moro-Martín et al. (2015) also reported the detection/non-detection of dust around stars of the DUNES and DEBRIS samples, based solely on their measurements of the *Herschel*/PACS 100 μm fluxes. Eight out of the 11 stars we claim as having excess match their positive detections, the exception being HIP 57757 for which they find a $\chi_{100} = 2.43$, and HIP 113283, for which we only detect excess at 160 μm, as pointed out above; HIP 88745 does not appear in their sample.

Since the observed excess emission of some disc candidates is relatively weak, one cannot exclude the possibility of contamination by background galaxies (E13, Krivov et al. 2013). Sibthorpe et al. (2013) carried out a cosmic variance independent measurement of the extragalactic number counts using PACS 100 μm data from the DEBRIS survey. To estimate the probability of galaxy source confusion in the study of debris discs, Table 2 of that paper gives the probabilities of one background source existing within a beam half-width half-maximum radius (3.4″for PACS 100, 5.8″for PACS 160) of the measured source location for a representative range of excess flux densities.

We have computed the excess flux densities at 100 and 160 μm for the 11 discs in Table 8. The smallest values at each wavelength occur for HIP 15510 (8.0 mJy) and HIP 113283 (7.8 mJy).

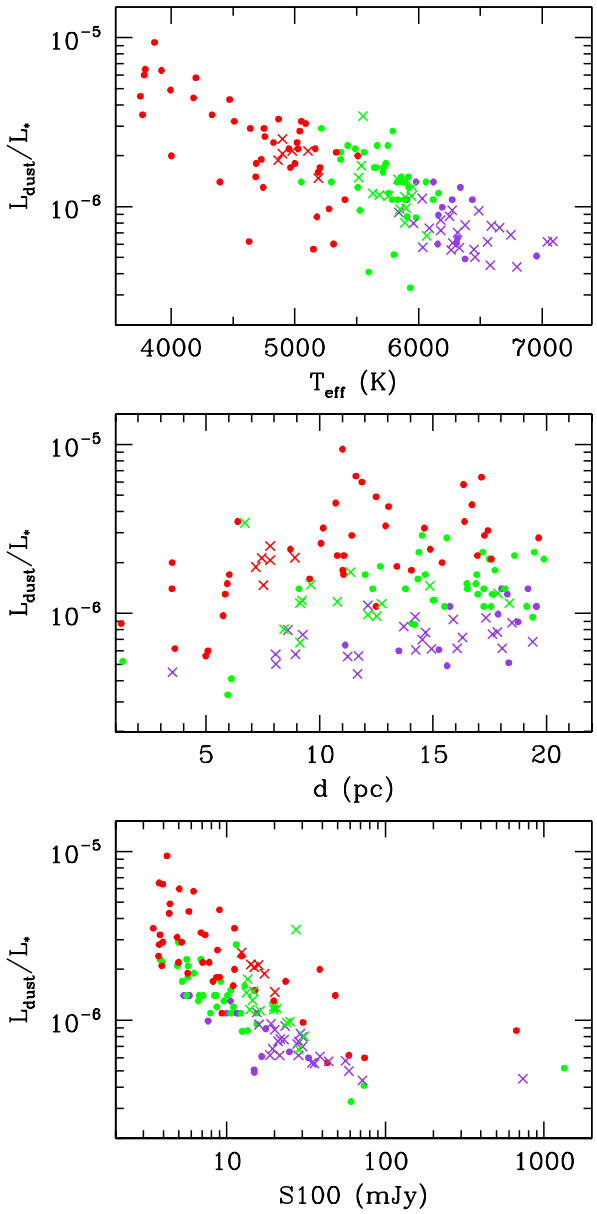

Fig. 4. Upper limits of the fractional luminosity of the dust for the non-excess sources of the DUNES_DB (crosses) and the DUNES_DU (dots) samples within 20 pc, plotted against the effective temperature, distance and stellar flux at 100 μm. Violet, green and red colours represent F, G and K stars. See text for details.

These values imply the probability of coincidental alignment with a background object of 0.2% and 1%, respectively. Since the excess flux densities are larger for the remaining targets, the probabilities for them are obviously lower.

In the case of a survey, it is more relevant to ask what is the probability that one or more members of the sample coincide with a galaxy. We have computed the median 1σ uncertainties – only considering the rms of the measurement, not the calibration error– of the PACS 100 and 160 μm fluxes for the set of 54 stars of the DUNES_DB sample within 20 pc, the results being 1.63 and 3.18 mJy respectively. Assuming fluxes for potential background sources of three times those σ values at the corresponding wavelengths, we obtain at 100 μm a chance of coincidental alignment for a single source in a sample of 54 stars of 1.1%.

Table 8. Black body dust temperatures and fractional dust luminosities for the DUNES_DB stars with excesses.

HIP	HD	SpT	T_{BB} (K)	R_{BB} (au)	L_{dust}/L_*
Stars with confirmed excesses					
5862	7570	F8 V	96	12	2.4×10^{-6}
15510 *	20794	G8 V	32	60	6.3×10^{-7}
16852 *	22484	F9 V	87	18	8.4×10^{-6}
23693	33262	F7 V	82	14	2.7×10^{-6}
57757	102870	F8 V	38	100	8.8×10^{-7}
61174 *	109085	F2 V	40	107	2.2×10^{-5}
64924 *	115617	G5 V	50	28	2.4×10^{-5}
71284	128167	F3 V	111	11	1.1×10^{-5}
88745 *	165908	F7 V	45	52	1.1×10^{-5}
113283	216803	K4 Vp	–	–	$< \mathit{2.0\times10^{-6}}$
116771	222368	F7 V	51	54	1.1×10^{-6}
Stars with χ_{100} and/or $\chi_{160}>3.0$ considered dubious excesses					
1599	1581	F9 V	18	264	9.6×10^{-7}
36366	58946	F0 V...	21	405	5.7×10^{-7}
37279	61421	F5 IV-V	113	16	1.5×10^{-6}
44248	76943	F5 V	27	243	4.6×10^{-7}
59199	105452	F0 IV-V	21	358	6.9×10^{-7}
61941	110379J	F0 V+...	30	248	3.3×10^{-7}
72659	131156	G8 V+K4 V	~40	40	2.9×10^{-6}
73695	133640	G2 V+G2 V	23	182	1.7×10^{-6}
77257	141004	G0 V	33	102	7.6×10^{-7}

Notes. * denotes that the source is extended. Modified black bodies were fitted for HIP 5862 and HIP 23693 to compute these excesses (see text for details); the T_{BB} listed in the table correspond to pure black bodies fitted excluding the PACS fluxes at 160 μm, the corresponding L_{dust}/L_* for those temperatures being 5.22×10^{-6} and 4.42×10^{-6} respectively. For HIP 61174 two black bodies were fitted to the warm and cold excesses, the warm excess corresponds to a T_{BB} = 300 K, which implies $L_{dust}/L_* = 1.65\times10^{-4}$. For HIP 113283 –a cold disc candidate– there is only one excess flux density at 160 μm, therefore a black body fit is not feasible; the value in italics for the upper limit of L_{dust}/L_* is just orientative and would correspond to a black body of 20 K normalized to the flux at 160 μm.

This implies the following probabilities $P(i)$ of having i fakes in the sample: $P(0)$=55%, $P(1)$=33%, $P(2)$=10%, $P(3)$=2% and $P(4)$=0.3%. For 160 μm, the chance of coincidental alignment of a single source is 2.9%, which implies $P(0)$=21%, $P(1)$=33%, $P(2)$=26%, $P(3)$=13% and $P(4)$=5%. Eq. (2) of the paper by Sibthorpe et al. (2013) and the matrices provided in that work were used for computing these estimates.

As we pointed out, five out of the 11 excess sources found in this work are spatially resolved, therefore we can consider them as real debris disc detections. According to the results above, the chances that the remaining six sources were all contaminated by background galaxies are ~ 0.003% and ~ 0.4% at 100 and 160 μm, respectively.

4.2. Stars without excesses

Fig. B.3 shows the SEDs of the DUNES_DB stars within 20 pc without excesses. In Fig. 4 the 3σ upper limits of the fractional luminosity of the dust for these sources are plotted as crosses

against the effective temperature, distance and stellar flux at 100 μm. For the sake of completeness, the non-excess DUNES_DU sources within 20 pc have been also added (dots, see Fig. 8 and Table 12 of E13). Violet, green and red colours represent F, G and K stars. The dubious sources are not included. The upper limits have been computed using the PACS 100 μm flux densities in the expression (4) by Beichman et al. (2006), with a representative $T_{\rm dust} = 50$ K.

The plots in Fig. 4 confirm and extend what was already seen in E13. The upper panel shows that the upper limits tend to decrease with $T_{\rm eff}$, the middle panel shows that for a given distance the hotter the star the lower the upper limit, and the lower panel shows that for a given predicted photospheric flux, which depends both on the spectral type and the distance, the upper limits increase with decreasing effective temperature. The general trend of the $L_{\rm dust}/L_*$ upper limits decreasing with the stellar temperature is expected just from pure black-body scaling considerations and the construction of the DUNES survey. Finer details, however, depend on the particular depth achieved for different spectral types and each individual observation.

The lowest values of the upper limits for the fractional luminosity reached are around $\sim 4.0 \times 10^{-7}$, the median for each spectral type been 7.8×10^{-7}, 1.4×10^{-6} and 2.2×10^{-6} for F, G and K stars respectively; the median for the whole sample is 1.4×10^{-6}.

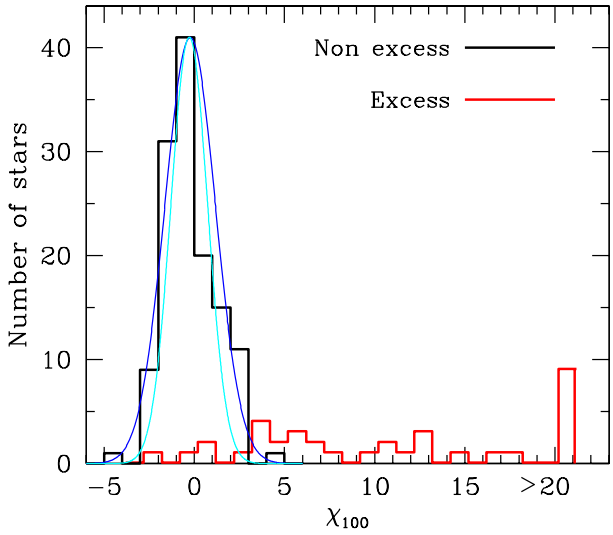

Fig. 5. Plotted in black, the histogram of the 100 μm significance χ_{100} for the non-excess sources of the merged DUNES_DU and DUNES_DB samples with $d \leq 20$ pc (dubious sources of both samples are not included). A Gaussian with $\sigma = 1.40$, the standard deviation of the χ_{100}-values for those sources, is plotted in blue. In cyan, we show a Gaussian with $\sigma = 1.02$, corresponding to the subsample of non-excess sources with $-2.0 < \chi_{100} < 2.0$. In red, the distribution of χ_{100} for the excess sources is also displayed. This figure is an extension of Fig. 6 of E13. See text for details.

In Fig. 5 histograms of the significance χ_{100} for the non-excess (black) and excess (red) sources of the merged DUNES_DU and DUNES_DB samples with $d \leq 20$ pc are plotted. For the non-excess sources, the mean, median and standard deviation of the χ_{100}-values are −0.23, −0.33 and 1.40, respectively. A Gaussian curve with $\sigma = 1.40$ is also plotted. These results are an extension of those already presented in Sect. 7.1 and Fig. 6 of E13, and are quantitatively very similar. The shift to the peak of the distribution to a negative value of χ_{100} likely reflects the fact that the extrapolation of the model photospheres to the PACS bands using a Rayleigh-Jeans approximation does not take into account the decrease in brightness temperature at ~100 μm that occurs in late-type stars, and therefore overestimates the photospheric emission around that wavelength. That was directly observed using DUNES data for α Cen A (Liseau et al. 2013) and α Cen B (Wiegert et al. 2014). Note that the stars in the red histogram with $\chi_{100} < 3.0$ are those considered as harbouring a cold disc, the excess being present only at 160 μm.

The fact that the standard deviation of the distribution departs from 1.0 –the expected value assuming a normal distribution– poses a problem already encountered in, e.g., E13 and Marshall et al. (2014). One potential origin of this could be the underestimation of the uncertainties either in the PACS 100 μm flux or in the photospheric predictions –or both– that would have the effect of increasing the absolute values of χ_{100}, since the term containing the uncertainties is in the denominator of the definition of χ_λ (eqn. 1). The distribution of χ_{100} would become broader, and σ would increase. We have done the experiment of computing the mean, median and σ for the non-excess sources considering only those stars with values of $-2.0 < \chi_{100} < 2.0$, the goal being to test the central part of the distribution. The results for the three quantities for this subset of stars (108 objects) are −0.28 (mean), −0.34 (median) and $\sigma = 1.02$ (Gaussian curve plotted in cyan in Fig. 5). This shows that the problem is more complex than dividing the stars into two bins of "excess" and "non-excess". There must be a spectrum of values with an increasing contribution from dust to the total measurement in the non-excess sample until it hits a threshold and becomes an excess value, that has been set in practice to $\chi_\lambda = 3.0$. This can have the effect of a departure of the full distribution from normal, while narrowing the interval of χ_{100}, ensuring that we deal with a more conservative definition of non-excess sources, seems to have the effect of approaching a normal distribution.

5. Analysis of the full DUNES sample

In E13 some conclusions were drawn based solely on the DUNES_DU subsample. In this section we will comment on the relevant results that are derived from the analysis of the merged DUNES_DU + DUNES_DB sample, both with $d \leq 15$ pc and $d \leq 20$ pc.

5.1. Excess incidence rates

Table 9 shows a summary of the excess incident rates in the DUNES_DU, DUNES_DB, and the full sample. In particular, the $d \leq 15$-pc subsample contains 23 F, 33 G and 49 K stars. The incidence rates of excesses are 0.26 (6 objects with excesses out of 23 F stars), 0.21 (7 out of 33 G stars) and 0. 20 (10 out of 49 K stars), the fraction for the total sample with $d \leq 15$ pc being 0.22 (23 out of 105 stars). Those percentages do not change significantly if we consider all targets within $d \leq 20$ pc. We also give the 95% confidence intervals for a binomial proportion for the corresponding counts according to the prescription by Agresti & Coull (1998).

As specified in Sect. 4.2, the median of the upper limits of the fractional luminosities per spectral type are 7.8×10^{-7}, 1.4×10^{-6} and 2.2×10^{-6} for F, G and K stars, respectively. As mentioned in E13, these numbers improve the sensitivity reached by *Spitzer* by one order of magnitude. Our results are to be compared with those found by Trilling et al. (2008) (see Table 4 of their paper), where the incidence rates of stars with excess at 70 μm, as measured by *Spitzer*/MIPS, are 0.18, 0.15 and 0.14 for F, G and K

Table 9. Summary of stars per spectral type in the DUNES_DU and DUNES_DB samples and frequency of excesses.

	F			G			K			FGK		
Sample	T	E	Frequency 95% interval	T	E	Frequency 95% interval	T	E	Frequency 95% interval	T	E	Frequency 95% interval
≤15 pc DUNES_DU	4	2	0.50 [0.15-0.85]	19	5	0.26 [0.11-0.49]	43	9	0.21 [0.11-0.35]	66	16	0.24 [0.15-0.36]
≤20 pc DUNES_DU	19	4	0.21 [0.08-0.44]	50	11	0.22 [0.13-0.35]	54	10	0.19 [0.10-0.31]	123	25	0.20 [0.14-0.28]
≤15 pc DUNES_DB	19	4	0.21 [0.08-0.44]	14	2	0.14 [0.03-0.41]	6	1	0.17 [0.01-0.58]	39	7	0.18 [0.09-0.33]
≤20 pc DUNES_DB	32	8	0.25 [0.13-0.42]	16	2	0.13 [0.02-0.37]	6	1	0.17 [0.01-0.58]	54	11	0.20 [0.12-0.33]
≤15 pc DUNES_DU+DUNES_DB	23	6	0.26 [0.12-0.47]	33	7	0.21 [0.10-0.38]	49	10	0.20 [0.11-0.34]	105	23	0.22 [0.15-0.31]
≤20 pc DUNES_DU+DUNES_DB	51	12	0.24 [0.14-0.37]	66	13	0.20 [0.12-0.31]	60	11	0.18 [0.10-0.30]	177	36	0.20 [0.15-0.27]
≤15 pc *Hipparcos*	23	6	0.26 [0.12-0.47]	42	*9*	0.21 *[0.11-0.36]*	89	*18*	0.20 *[0.13-0.30]*	154	*33*	*0.21 [0.16-0.29]*

Note: "T" and "E" mean "Total" and "Excess", respectively.

stars respectively. The variation of the incidence rates with spectral type is likely directly related to the dependence of the fractional luminosity with $T_{\rm eff}$ (see Fig. 4).

As we showed in Sect. 2.2, the merged sample with $d \leq 15$ pc analysed in this paper is complete for F stars, almost complete for G stars, whereas a number of K stars are lost from the parent set of the *Hipparcos* catalogue from which the final DUNES sample was drawn, the reason being the observational constraint imposed (background contamination, see Sect. 2.1). In the lowest row of Table 9, we give the expected total number of stars of each spectral type in the *Hipparcos* catalogue with $d \leq 15$ pc that would show excess, under the assumption that the individual excess frequencies are those obtained from the full DUNES sample; the numbers that are extrapolations for the G and K stars are written in italics. The total incidence rate of excesses for the *Hipparcos* subset, namely $0.21^{+0.08}_{0.05}$, does not change with respect to the DUNES result, $0.22^{+0.09}_{-0.07}$, the confidence interval being obviously slightly narrower. Since both τ Cet and ϵ Eri are within 15 pc and have debris discs (Lawler et al. 2014, Greaves et al. 2014), should these sources be included in the statistics, the total incidence rate of excesses within $d \leq 15$ pc would be $0.23^{+0.09}_{-0.07}$ (25 out of 107 objects).

The results on the incidence rates of excesses from PACS data allows us to push the distribution found from MIPS data, whose minimum detection limit was $L_{\rm dust}/L_* \simeq 4 \times 10^{-6}$ (Bryden et al. 2006), down to minimum detections around 4×10^{-7}. Fig. 6 shows a cumulative distribution, plotted in black, of the frequency of excess detections from PACS data as a function of the fractional dust luminosity. The steepness of the distribution decreases at luminosities lower than $\sim 4 \times 10^{-6}$. The extrapolation of a straight line (in green) fitted to the bins at the left of that value predicts an incidence of excesses ~ 0.25 at $L_{\rm dust}/L_* = 10^{-7}$, the current estimate of the Kuiper-belt dust fractional luminosity (Vitense et al. 2012). Plotted in cyan, the cumulative distribution of the frequency of excesses derived from the results shown in Tables 2 and 3 of Bryden et al. (2006) (11 excesses out of 73 stars) is also included in Fig. 6; these were obtained from *Spitzer*/MIPS observations at 70 μm, with a detection limit of $L_{\rm dust}/L_* \simeq 4\times10^{-6}$. The shape of both distributions is roughly the same in the range $\sim 4\times10^{-6} - 3\times10^{-5}$. A straight line (in red) fitted to the bins of our cumulative histogram in that region would predict a larger incidence of excesses ~ 0.35, at fractional luminosities of 10^{-7}. A very similar prediction (~ 0.32) is obtained from the cumulative histogram by Bryden et al. (2006).

The fact that the *Spitzer*/MIPS and *Herschel*/PACS distributions are close to each other in the overlapping range of luminosities is more than a simple consistency check. The similarity might indicate that the dust temperature does not correlate with the dust luminosity in that range. Indeed, the dust fractional luminosities in Bryden et al. (2006) were based either on a single 70 μm measurement or on a combination of 24 μm and 70 μm fluxes. The dust luminosities in this work were derived from fluxes at longer wavelengths, basically from 70 μm, 100 μm, and 160 μm PACS fluxes. For simplicity, let us assume that the Spitzer luminosities were based solely on a 70 μm flux and the Herschel ones on a 100 μm flux only. Under this assumption, the fractional luminosity is directly proportional to the flux at 70 μm or 100 μm (see eqn. 3 in Bryden et al. 2006). Next, it is obvious that the F70/F100 ratio decreases with the decreasing dust temperature. Should the discs with lower fractional luminosities be systematically colder, the F70/F100 flux ratio would decrease with the dust luminosity. This would make the histogram based on F70 flux flatter and conversely, the histogram based on the F100 flux steeper. In the opposite case, i.e. if the discs of low fractional luminosity were systematically warmer, the opposite would be true. In either case, the slopes of the two histograms would differ, but this is not what we see in Fig. 6; instead, they are nearly the same in the $\sim 4\times10^{-6} - 3\times10^{-5}$ luminosity range. Therefore, the dust temperature should be nearly the same for all discs with the dust luminosities in that range.

What implications might this have? The dust temperature is directly related to the disc radius. Assuming that the average stellar luminosity of all stars with discs in that fractional luminosity range is nearly the same, the fact that the dust temperature does not depend on the dust luminosity would automatically mean that the disc radius does not depend on the dust luminosity either.

This would imply that it is not the location of the dust-producing planetesimals that primarily determines the disc dustiness. Instead, the disc dustiness must be set by other players in the system, e.g. by the dynamical evolution of presumed planets in the disc cavity.

The bottom line of this analysis is that the flattening of the distribution at low values of $L_{\rm dust}/L_*$, provided by the results of the *Herschel* observations, decreases drastically the predictions of the excess incidence rate at luminosities $\sim 10^{-7}$ compared to those obtained from MIPS results.

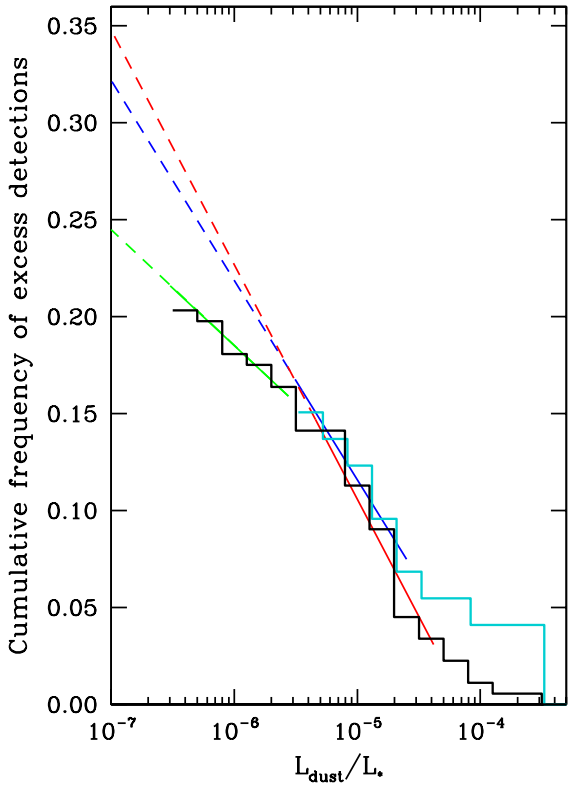

Fig. 6. Cumulative distributions of the frequency of excesses obtained in this work (black) and those obtained from *Spitzer*/MIPS results (Bryden et al. 2006) (cyan), both plotted against fractional dust luminosity. The green straight line is a fit to the values of the frequencies at the less steep part of our cumulative distribution. The extrapolation down to 10^{-7}, the current estimate of the Kuiper-belt fractional luminosity, gives a prediction for the incidence rate of excesses of ~ 0.25. The extrapolation from a straight line, plotted in red, fitted to the steeper part of the distribution, that would mimic the MIPS results, gives a higher prediction ~ 0.35. The prediction from Bryden et al. (2006) distribution, from the blue straight-line fit, is ~ 0.32. See text for details.

5.2. Debris discs/binarity

Fig. 7 shows the projected binary separation versus disc radius for excess sources in those stars catalogued as binaries in Table 4 of this work (red symbols) as well as those in E13 (Table 16 of that paper, blue symbols). Squares and diamonds represent confirmed and dubious excess sources, respectively; triangles mark the spectroscopic binary HIP 77257, which has an unknown –but presumably small– separation. Filled and open symbols connected with an arrow represent the black-body disc radius, $R_{\rm BB}$ computed using eqn. (2) and a more realistic disc radius estimate, $R_{\rm dust}$, according to Pawellek & Krivov (2015), respectively, for the same system[11].

The discs above the diagonal straight line would be circumprimary, those below the line circumbinary. The grey area roughly marks the discs that are not expected to exist as they would be disrupted by the gravity of the companion (assuming the true distance to be close to the projected one). There is no any apparent reason why all the red symbols, which correspond to stars in the DUNES_DB sample, lie in the "circumbinary" region. The ranges of the disc radii in DUNES_DU and DUNES_DB are similar, it is only the distributions of the binary separations that are different (more wide binaries in the DUNES_DU sample); whether one finds a wide or a close binary among the excess sources in one or another sample seems to be purely accidental.

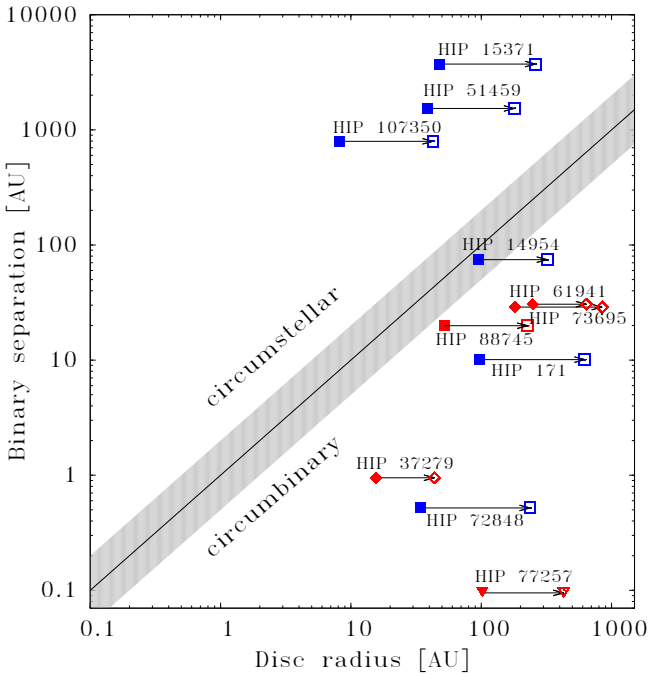

Fig. 7. Projected binary separation plotted against disc radius for excess sources in those stars catalogued as binaries. Red and blue symbols represent objects studied in this work and in E13, respectively. Squares and diamonds are confirmed or dubious excesses. Filled and open symbols represent the value of $R_{\rm BB}$ and $R_{\rm dust}$ (see text for details). The inverted triangles at the bottom represent the binary HIP 77257 for which the separation is not known.

5.3. Debris discs/metallicity

In Fig. 8, the fractional luminosities $L_{\rm dust}/L_*$ (for the excess sources) and the upper limits (non-excess sources) for the full DUNES sample with $d \leq 20$ pc, are plotted against stellar metallicity. It is interesting to note that whereas above the mean metal abundance of the whole sample, $[{\rm Fe/H}]_{\rm mean}=-0.11$, we find a wide range of values of the fractional luminosity, covering more than two orders of magnitude, the discs around stars with [Fe/H] below -0.11 seem to show a much narrower interval of $L_{\rm dust}/L_*$, around $\sim 10^{-5}$. Two statistical tests performed on the data, namely the Kolmogorov-Smirnov and the Anderson-Darling, state that the result is not statistically significant; there-

[11] Assuming a composition of astrosilicate (50%) and ice (50%), $\Gamma = 5.42\,(L_*/L_\odot)^{-0.35}$, $R_{\rm dust} = \Gamma\, R_{\rm BB}$.

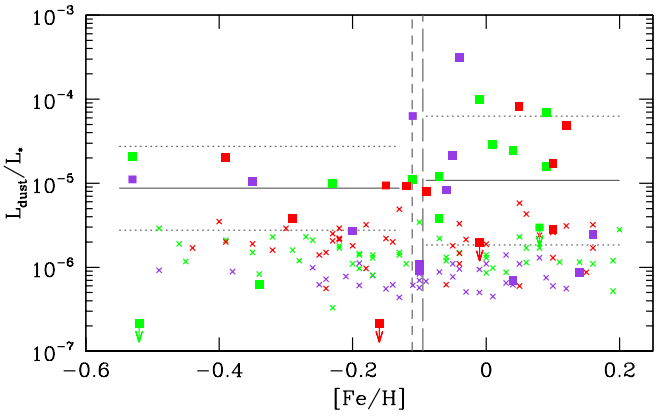

Fig. 8. Fractional dust luminosities $L_{\rm dust}/L_*$ for the DUNES_DU and DUNES_DB stars with excesses (squares) and $d \leq 20$ pc (Table 14 of E13 and Table 8 of this work), and upper limits for the non-excess sources (crosses), all of them plotted against metallicity, [Fe/H]. F, G and K stars are plotted in violet, green and red. The short-dashed vertical line marks the mean metal abundance of the whole sample, [Fe/H]=−0.11, whereas the long-dashed line marks the median, [Fe/H]=−0.095. The horizontal lines mark the means (solid) of the fractional luminosities for the debris discs of stars showing excess, with [Fe/H]≤ −0.11 and > −0.11, and plus and minus their standard errors (dotted), defined as $\sigma/\sqrt{n}$, where σ is the standard deviation; these computations have been done over the values of $\log(L_{\rm dust}/L_*)$.

fore a larger sample would be needed to confirm or discard this trend.

Greaves et al. (2006) and Beichman et al. (2006) found that the incidence of debris discs was uncorrelated with metallicity, these results being confirmed by Maldonado et al. (2012, 2015) who found no significant differences in metallicity, individual abundances or abundance-condensation temperature trends between stars with debris discs and stars with neither debris nor planets. However, Maldonado et al. (2012) pointed out that there could be a deficit of stars with discs at very low metallicities ($-0.50 < [{\rm Fe/H}] < -0.20$) with respect to stars without detected discs. A recent work by Gáspár et al. (2016), where the correlation between metallicity and debris disc mass is studied, confirmed the finding by Maldonado et al. (2012) of a deficit of debris-disc-bearing stars over the range $-0.5 \leq [{\rm Fe/H}] \leq -0.2$. Out of the full sample analysed in this paper, 166 stars have determination of their metallicities, all of them are plotted in Fig. 8; the number of stars with excesses at both sides of the median metallicity, $[{\rm Fe/H}]_{\rm median}$=−0.095, is 16 ([Fe/H]< −0.095) and 20 ([Fe/H]> −0.095), i.e. an slighly lower proportion in the low-metallicity side. Considering an average uncertainty of ±0.05 dex in the metallicities, that could move objects from one to the other side of the boundary marked by the median, we can count the number of debris discs around stars with metallicities lower than $[{\rm Fe/H}]_{\rm median} - 0.05$ and higher than $[{\rm Fe/H}]_{\rm median} + 0.05$, the results being 11/83 and 15/83 objects respectively. The fractions are $0.13^{+0.09}_{-0.06}$ and $0.18^{+0.10}_{-0.07}$, respectively, with the uncertainties corresponding to a 95% confidence level. Although this result is still not statistically significant, it points in the same direction as the ones hinted by Maldonado et al. (2012) and confirmed by Gáspár et al. (2016).

5.4. Evolutionary considerations

Fig. 9 shows a plot of $\log R'_{\rm HK}$ against $(B–V)$ for the DUNES stars within 20 pc, plotted as cyan squares. The stars with excesses are plotted as diamonds with sizes proportional to $\log L_{\rm dust}/L_*$. The regions separating "very inactive", "inactive", "active" and "very active" stars, proposed by Gray et al. (2006) (see their Fig. 4), are also indicated. This diagram is a qualitative evolutionary picture of FGK main sequence stars in the sense that as the stars evolve, their rotation rates decrease as a consequence of angular momentum loss and therefore, their levels of chromospheric activity also decrease (see e.g. Skumanich (1972), Noyes et al. (1984), Rutten (1987)).

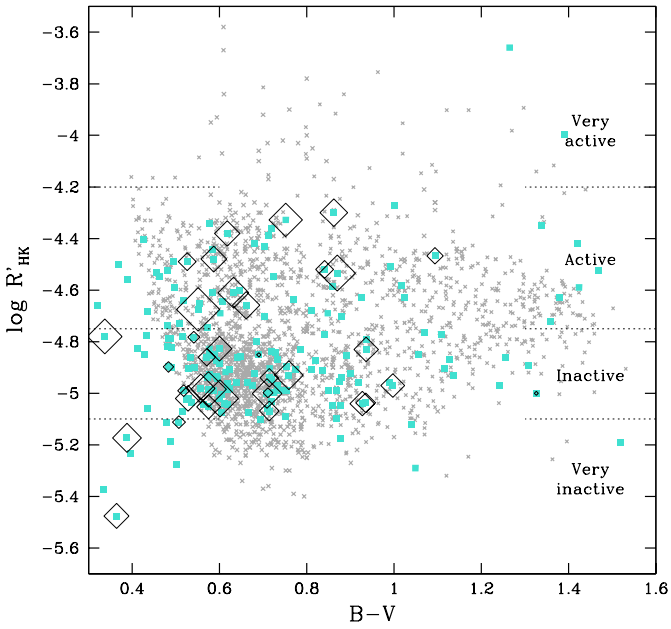

Fig. 9. A diagram $\log R'_{\rm HK} - (B–V)$ showing the stars of the full DUNES sample with $d \leq 20$ pc (cyan squares). The stars identified to have far-IR excess in E13 and in this paper are plotted as diamonds with a size proportional to the value of the fractional dust luminosity. In grey, in the background, the samples of data by Henry et al. (1996) and Gray et al. (2006).

Out of the 177 stars of the DUNES sample with $d \leq 20$ pc, 175 have $\log R'_{\rm HK}$ data; 119 objects (25 showing excesses, 21.0%) are in the region of "inactive" or "very inactive" stars, $\log R'_{\rm HK} < -4.75$, "old" objects, whereas 56 (11 with excesses, 19.6%) are in the region of the "active" or "very active" stars $\log R'_{\rm HK} > -4.75$, "young" objects, therefore, the incidence of debris discs is similar among inactive or active stars.

The uneven distribution of stars below and above the activity gap is more apparent if we use large samples of field FGK stars to check the relative abundance of active and inactive objects in the solar neighbourhood. Two catalogues have been used to ascertain this point: Henry et al. (1996) catalogue contains 814 southern stars within 50 pc; most of them were chosen to be G dwarfs. From the Gray et al. (2006) catalogue, which contains stars within 40 pc, we have retained those FGK stars with luminosity classes V or V-IV, amounting 1270 objects. The stars of both surveys have been plotted as grey crosses in Fig. 9. The bimodal distribution in stellar activity first noted by Vaughan & Preston (1980) in a sample of northern objects is seen in both catalogues, the percentage of inactive stars be-

Table 10. Statistics of the dust fractional luminosities.

	$L_{\rm dust}/L_*$			
	Mean	Median	MAD	N
$\log R'_{\rm HK} > -4.75$ (active)	$(5.3 \pm 3.0) \times 10^{-5}$	1.7×10^{-5}	1.3×10^{-5}	10
$\log R'_{\rm HK} < -4.75$ (inactive)	$(1.8 \pm 0.6) \times 10^{-5}$	9.3×10^{-6}	8.3×10^{-6}	22
$P_{\rm rot} < 10$ d	$(5.0 \pm 3.7) \times 10^{-5}$	1.2×10^{-5}	9.7×10^{-6}	8
10 d $< P_{\rm rot} <$ 30 d	$(2.9 \pm 1.0) \times 10^{-5}$	1.4×10^{-5}	1.1×10^{-5}	12
$P_{\rm rot} > 30$ d	$(9.9 \pm 2.9) \times 10^{-6}$	8.6×10^{-6}	4.8×10^{-6}	8

Notes. The uncertainties in the means are the standard errors defined as $\sigma/\sqrt{n}$, where σ is the standard deviation. MAD (Median Absolute Deviation) is defined as MAD=`median[abs(x-median(x))]` for a vector `x`.

low the gap frontier, placed at $\log R'_{\rm HK} = -4.75$ being 73% (Henry et al. 1996), and 64% (Gray et al. 2006) for $B-V<0.85$. For the sample in this paper, the percentage of stars below $\log R'_{\rm HK} = -4.75$ is 68%.

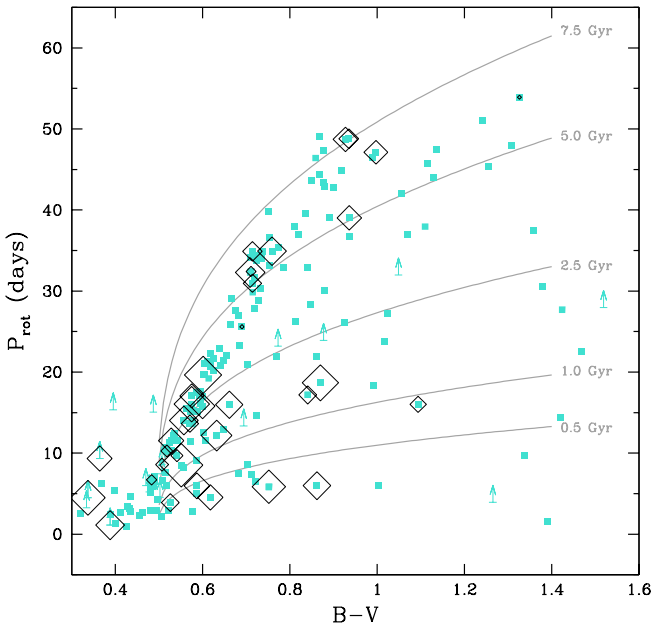

Fig. 10. A diagram $P_{\rm rot} - (B-V)$ showing the stars of the full DUNES sample with $d \leq 20$ pc (cyan squares). As in Fig. 9 the stars identified to have far-infrared excesses are plotted as diamonds with a size proportional to the value of the fractional dust luminosity. Superimposed, five "gyrochrones" computed following Mamajek & Hillenbrand (2008) (see Appendix A of this work).

Fig. 10 shows the rotation periods (see Table 3) plotted against the $(B-V)$ colours for the DUNES stars within 20 pc. Five "gyrochrones" corresponding to 0.6, 1.0, 2.5, 5.0 and 7.5 Gyr, computed according to Mamajek & Hillenbrand (2008) are also included in the graph. The stars with excesses are plotted as black diamonds with sizes proportional to $\log(L_{\rm dust}/L_*)$. In spite of the problems involved in the estimation of ages, the reliability of the computation of rotation periods from the chromospheric activity indicator $\log R'_{\rm HK}$ (see Appendix A), makes this diagram a reliable evolutionary scenario of how the sample and the excess sources are distributed.

In Fig. 9 it is fairly apparent that the sizes of the diamonds above the line $\log R'_{\rm HK} = -4.75$ are, on average, larger than those below; the line separates active (younger) from inactive (older) stars. In turn, in Fig. 10 it can be also seen that the average sizes of the symbols decrease as the rotation periods increase, therefore suggesting a decreasing fractional luminosity with increasing stellar age.

To quantify this, we have taken two bins in chromospheric activity, namely stars above and below $\log R'_{\rm HK} = -4.75$, and three bins in rotation period, $P_{\rm rot} < 10$ d, 10 d$< P_{\rm rot} <$ 30 d, and $P_{\rm rot} > 30$ d, and have determined means and medians of the dust fractional luminosities of the stars in each bin. The results of this exercise can be seen in Table 10 where the calculations have been carried out for the whole sample ($d \leq 20$ pc). Stars with upper limits in $L_{\rm dust}/L_*$ (three objects in the DUNES_DU sample and one in DUNES_DB) and with lower limits in $P_{\rm rot}$ (four objects) have not been included; in the last column N specifies the number of stars used in each case. The effects of decreasing $L_{\rm dust}/L_*$ with decreasing activity and increasing rotation period are apparent. These results point to the fact that as the stars get older, there seems to be a slow erosion of the mass reservoir and dust content in the disc, with the effect of a decrease in $L_{\rm dust}/L_*$.

6. Summary

The main goal of this paper –and of the DUNES project– is to study the incidence of debris discs around FGK stars in the solar neighbourhood. Data obtained with the ESA *Herschel* space observatory have been used to characterize the far-IR SED of a sample of objects observed during two Open Time Key Programmes, namely DUNES and DEBRIS. A sample of 177 stars within 20 pc has been analysed.

Fig. 11 shows the fractional dust luminosity, $L_{\rm dust}/L_*$, plotted against the dust temperature, $T_{\rm dust}$, for the 36 stars for which a far-IR excess has been detected (see Table 14 of E13 and Table 8 of this work). The detection limits for a G5 V star at 20 pc, following Bryden et al. (2006), are also included in the graph; the assumed 1σ fractional flux accuracies are 20% for *Spitzer*/MIPS at 70 μm and 10% for *Herschel*/PACS at 100 μm (i.e. S/N=10). 14 stars are located below the MIPS 70 μm curve, showing how *Herschel*/PACS has pushed the limits down to fractional luminosities a few times that of the Kuiper-belt.

A summary of the main results follows:

1. *Herschel*/PACS photometry –complemented in some cases with SPIRE data– are provided for the so-called DUNES_DB sample, a set of 54 stars (32 F, 16 G and 6 K) observed by DEBRIS for the DUNES consortium. Parameters, ancillary photometry and details on the multiplicity are also given. The DUNES_DU sample was already analysed in detail in E13. See Sect. 2, Tables 2–5, and 7.

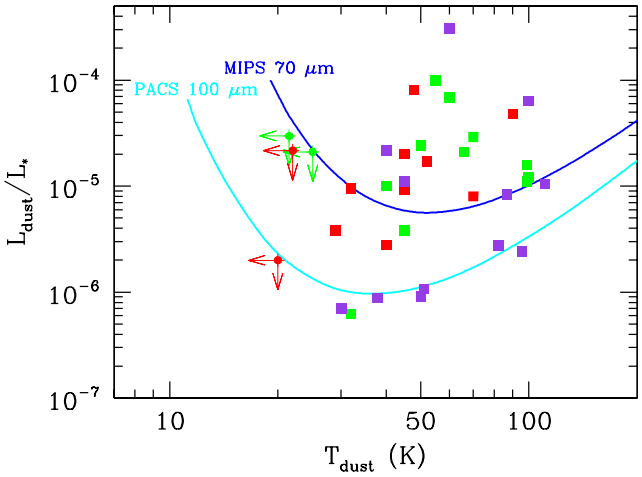

Fig. 11. A diagram $L_{\rm dust}/L_* - T_{\rm dust}$ showing the position of the 36 stars, out of the 177 in the DUNES sample within 20 pc, for which an excess has been detected at far-IR wavelengths. F, G and K stars are plotted in violet, green and red. The detection limits for a G5 V star at 20 pc for PACS 100 μm and MIPS 70 μm are also included.

2. Eleven sources of the DUNES_DB sample show excesses in the PACS 100 and/or 160 μm bands (i.e. χ_{100} and/or $\chi_{160} > 3.0$). Five of them are spatially resolved: four were previously known, whereas HIP 16852 is a new addition to the list of extended sources. This object appears marginally resolved. See Tables 7 and 8, and Sect. 4.1.
3. The DUNES sample –merger of DUNES_DU and DUNES_DB– with $d \leq 15$ pc (105 stars) is complete for F stars and almost complete for G stars. The number of K stars is large enough to provide a solid estimate of the fraction of stars with discs for this spectral type. See Sect. 2.2.
4. The DUNES $d \leq 15$-pc subsample contains 23 F, 33 G and 49 K stars. The incidence rates of debris discs per spectral type are $0.26^{+0.21}_{-0.14}$ (6 objects with excesses out of 23 F stars), $0.21^{+0.17}_{-0.11}$ (7 out of 33 G stars) and $0.20^{+0.14}_{-0.09}$ (10 out of 49 K stars), the fraction for all three spectral types together being $0.22^{+0.08}_{-0.07}$ (23 out of 105 stars). Should τ Cet and ϵ Eri –not belonging to the DUNES sample– be included in the statistics, the total incidence rate of excesses for stars within $d \leq 15$ pc would be $0.23^{+0.09}_{-0.07}$ (25 out of 107 objects). See Sect. 5.1 and Table 9.
5. The lowest values of the upper limits for the fractional luminosity, $L_{\rm dust}/L_*$, reached are around $\sim 4.0 \times 10^{-7}$ the median for the whole sample being 1.4×10^{-6}. These numbers are a gain of one order of magnitude compared with those provided by *Spitzer* (see Sect. 4.2). Although it may seem obvious, we must stress the fact that the excess detection rates reported in this paper are sensitivity limited, therefore, they still represent lower limits of the *actual* incidence rates. See Sect. 5.1 and the discussion on Fig. 6.
6. There are hints of a different behaviour in the fractional luminosities of the discs at lower metallicities and higher metallicities, if we split the sample around $[{\rm Fe/H}]_{\rm mean} = -0.11$: the former seem to cover a narrower interval of fractional luminosities than the latter ones. Splitting around the median $[{\rm Fe/H}]]_{\rm median} = -0.095$ the sample of stars with determinations of metallicities available (166 objects), there seems to be a slight deficit of debris discs at lower metallicities (16 discs out of 83 stars), when compared to the number at higher metallicities (20 discs out of 83 stars). See Sect. 5.3, and Fig. 8.
7. Regarding the chromospheric activity, the incidence of debris discs is similar among inactive and active stars. There is a decrease of the average $L_{\rm dust}/L_*$ with decreasing activity/increasing rotation period. Since the stellar activity and the spin-down are proxies of the age, this result points to the fact that as the stars get older, there seems to be a slow dilution of the dust in the disc with the effect of a decrease in its fractional luminosity. See Sect. 5.4 and Figs. 9 and 10.

Acknowledgements. The authors are gratefuly to the referee for the careful revision of the original manuscript, comments and suggestions. We also thank Francisco Galindo, Mauro López del Fresno and Pablo Rivière for their valuable help. B. Montesinos and C. Eiroa are supported by Spanish grant AYA2013-45347-P; they and J.P. Marshall and J. Maldonado were supported by grant AYA2011-26202. A.V. Krivov acknowledges the DFG support under contracts KR 2164/13-1 and KR 2164/15-1. J. P. Marshall is supported by a UNSW Vice-Chancellor's postdoctoral fellowship. R. Liseau thanks the Swedish National Space Board for its continued support. A. Bayo acknowledges financial support from the Proyecto Fondecyt de Iniciación 11140572 and scientific support from the Millenium Science Initiative, Chilean Ministry of Economy, Nucleus RC130007. J.-C. Augereau acknowledges support from PNP and CNES. F. Kirchschlager thanks the DFG for finantial support under contract WO 857/15-1. C. del Burgo has been supported by Mexican CONACyT research grant CB-2012-183007.

References

Agresti, A., & Coull, B. A. 1998, The American Statistician, 52, 119
Armitage, P. J. 2015, arXiv:1509.06382
Aumann, H. H., Beichman, C. A., Gillett, F. C., et al. 1984, ApJ, 278, L23
Aumann, H. H., & Probst, R. G. 1991, ApJ, 368, 264
Backman, D. E., & Paresce, F. 1993, Protostars and Planets III, 1253
Balog, Z., Müller, T., Nielbock, M., et al. 2014, Experimental Astronomy, 37, 129
Baliunas, S., Sokoloff, D., & Soon, W. 1996, ApJ, 457, L99
Barnes, S. A. 2007, ApJ, 669, 1167
Beichman, C. A., Bryden, G., Stapelfeldt, K. R., et al. 2006, ApJ, 652, 1674
Bertone, E., Buzzoni, A., Chávez, M., & Rodríguez-Merino, L. H. 2004, AJ, 128, 829
Bessell, M. S. 1979, PASP, 91, 589
Brott, I. & Hauschildt, P. H. 2005, in ESA Special Publication, Vol. 576, The Three-Dimensional Universe with Gaia, ed. C. Turon, K. S. O'Flaherty, & M. A. C. Perryman, 565
Bryden, G., Beichman, C. A., Trilling, D. E., et al. 2006, ApJ, 636, 1098
Carter, B. S. 1990, MNRAS, 242, 1
Castelli, F. & Kurucz, R. L. 2003, in IAU Symposium, Vol. 210, Modelling of Stellar Atmospheres, ed. N. Piskunov, W. W. Weiss, & D. F. Gray, 20P
Chen, C. H., Mittal, T., Kuchner, M., et al. 2014, ApJS, 211, 25
Cohen, M., Wheaton, W. A., & Megeath, S. T. 2003, AJ, 126, 1090
Cutri, R. M., & et al. 2012, VizieR Online Data Catalog, 2311,
Cutri, R. M., & et al. 2013, VizieR Online Data Catalog, 2328,
Decin, G., Dominik, C., Waters, L. B. F. M., & Waelkens, C. 2003, ApJ, 598, 636
Duchêne, G., Arriaga, P., Wyatt, M., et al. 2014, ApJ, 784, 148
Duncan, D. K., Vaughan, A. H., Wilson, O. C., et al. 1991, ApJS, 76, 383
Eiroa, C., Marshall, J. P., Mora, A., et al. 2011, A&A, 536, L4
Eiroa, C., Marshall, J. P., Mora, A., et al. 2013, A&A, 555, AA11
Elias, J. H., Frogel, J. A., Matthews, K., & Neugebauer, G. 1982, AJ, 87, 1029
Epstein, C. R., & Pinsonneault, M. H. 2014, ApJ, 780, 159
Ertel, S., Wolf, S., Marshall, J. P., et al. 2012, A&A, 541, A148
Flower, P. J. 1996, ApJ, 469, 355
Fuhrmann, K. 2008, MNRAS, 384, 173
Gáspár, A., Rieke, G. H., & Balog, Z. 2013, ApJ, 768, 25
Gáspár, A., Rieke, G. H., & Ballering, N. 2016, http://arxiv.org/abs/1604.07403
Gezari, D. Y., Patricia S. Pitts, P. S., & Schmitz, M. 2000, Catalog of Infrared Observations, Version 5.1.
Glass, I. S. 1975, MNRAS, 171, 19P
Gray, R. O. 1998, AJ, 116, 482
Gray, R. O., Corbally, C. J., Garrison, R. F., McFadden, M. T., & Robinson, P. E. 2003, AJ, 126, 2048
Gray, R. O., Corbally, C. J., Garrison, R. F., et al. 2006, AJ, 132, 161
Greaves, J. S., Fischer, D. A., & Wyatt, M. C. 2006, MNRAS, 366, 283
Greaves, J. S., Sibthorpe, B., Acke, B., et al. 2014, ApJ, 791, L11
Griffin, M. J., Abergel, A., Abreu, A., et al. 2010, A&A, 518, L3

Gustafsson, B., Edvardsson, B., Eriksson, K., et al. 2008, A&A, 486, 951
Habing, H. J., Dominik, C., Jourdain de Muizon, M., et al. 2001, A&A, 365, 545
Hall, J. C., Lockwood, G. W., & Skiff, B. A. 2007, AJ, 133, 862
Hauck, B., & Mermilliod, M. 1997, VizieR Online Data Catalog, 2215,
Hauck, B., & Mermilliod, M. 1998, A&AS, 129, 431
Henry, T. J., Soderblom, D. R., Donahue, R. A., & Baliunas, S. L. 1996, AJ, 111, 439
Holmberg, J., Nordström, B., & Andersen, J. 2009, A&A, 501, 941
Kennedy, G. M., Wyatt, M. C., Sibthorpe, B., et al. 2012, MNRAS, 421, 2264
Kennedy, G. M., Matrà, L., Marmier, M., et al. 2015, MNRAS, 449, 3121
Koornneef, J. 1983, A&AS, 51, 489
Krivov, A. V. 2010, Research in Astronomy and Astrophysics, 10, 383
Krivov, A. V., Eiroa, C., Löhne, T., et al. 2013, ApJ, 772, 32
Kroupa, P. 2001, MNRAS, 322, 231
Lawler, S. M., Di Francesco, J., Kennedy, G. M., et al. 2014, MNRAS, 444, 2665
Liseau, R., Montesinos, B., Olofsson, G., et al. 2013, A&A, 549, L7
Maldonado, J., Martínez-Arnáiz, R. M., Eiroa, C., Montes, D., & Montesinos, B. 2010, A&A, 521, A12
Maldonado, J., Eiroa, C., Villaver, E., Montesinos, B., & Mora, A. 2012, A&A, 541, A40
Maldonado, J., Eiroa, C., Villaver, E., Montesinos, B., & Mora, A. 2015, A&A, 579, A20
Mamajek, E. E., & Hillenbrand, L. A. 2008, ApJ, 687, 1264
Marshall, J. P., Krivov, A. V., del Burgo, C., et al. 2013, A&A, 557, A58
Marshall, J. P., Moro-Martín, A., Eiroa, C., et al. 2014, A&A, 565, A15
Martínez-Arnáiz, R., Maldonado, J., Montes, D., Eiroa, C., & Montesinos, B. 2010, A&A, 520, A79
Matthews, B. C., Sibthorpe, B., Kennedy, G., et al. 2010, A&A, 518, L135
Matthews, B. C., Krivov, A. V., Wyatt, M. C., Bryden, G., & Eiroa, C. 2014, Protostars and Planets VI, 521
Meibom, S., Barnes, S. A., Platais, I., et al. 2015, Nature, 517, 589
Montesinos, B., Thomas, J. H., Ventura, P., & Mazzitelli, I. 2001, MNRAS, 326, 877
Moro-Martín, A., Marshall, J. P., Kennedy, G., et al. 2015, ApJ, 801, 143
Mustill, A. J., Veras, D., & Villaver, E. 2014, MNRAS, 437, 1404
Noyes, R. W., Hartmann, L. W., Baliunas, S. L., Duncan, D. K., & Vaughan, A. H. 1984, ApJ, 279, 763
Ott, S. 2010, Astronomical Data Analysis Software and Systems XIX, 434, 139
Pawellek, N., & Krivov, A. V. 2015, MNRAS, 454, 3207
Pecaut, M. J., & Mamajek, E. E. 2013, ApJS, 208, 9
Pepe, F., Lovis, C., Ségransan, D., et al. 2011, A&A, 534, A58
Perryman, M. A. C., Lindegren, L., Kovalevsky, J., et al. 1997, A&A, 323, L49
Phillips, N. M., Greaves, J. S., Dent, W. R. F., et al. 2010, MNRAS, 403, 1089
Pilbratt, G. L., Riedinger, J. R., Passvogel, T., et al. 2010, A&A, 518, L1
Poglitsch, A., Waelkens, C., Geis, N., et al. 2010, A&A, 518, L2
Roberge, A., Kamp, I., Montesinos, B., et al. 2013, ApJ, 771, 69
Rutten, R. G. M. 1987, A&A, 177, 131
Saffe, C., Gómez, M., & Chavero, C. 2005, A&A, 443, 609
Salpeter, E. E. 1955, ApJ, 121, 161
Santos, N. C., Israelian, G., & Mayor, M. 2004, A&A, 415, 1153
Selby, M. J., Hepburn, I., Blackwell, D. E., et al. 1988, A&AS, 74, 127
Sibthorpe, B., Ivison, R. J., Massey, R. J., et al. 2013, MNRAS, 428, L6
Skiff, B. A. 2009, VizieR Online Data Catalog, 1, 2023
Skumanich, A. 1972, ApJ, 171, 565
Soderblom, D. R. 2010, ARA&A, 48, 581
Sousa, S. G., Santos, N. C., Mayor, M., et al. 2008, A&A, 487, 373
Suárez Mascareño, A., Rebolo, R., González Hernández, J. I., & Esposito, M. 2015, arXiv:1506.08039
Takeda, Y., Ohkubo, M., Sato, B., Kambe, E., & Sadakane, K. 2005, PASJ, 57, 27
Torres, G. 2010, AJ, 140, 1158
Turon, C., Gomez, A., Crifo, F., et al. 1992, A&A, 258, 74
Trilling, D. E., Bryden, G., Beichman, C. A., et al. 2008, ApJ, 674, 1086
Valenti, J. A. & Fischer, D. A. 2005, ApJS, 159, 141
Vaughan, A. H., & Preston, G. W. 1980, PASP, 92, 385
van Leeuwen, F. 2007, A&A, 474, 653
Vitense, C., Krivov, A. V., Kobayashi, H., & Löhne, T. 2012, A&A, 540, A30
Vogt, S. S., Wittenmyer, R. A., Butler, R. P., et al. 2010, ApJ, 708, 1366
Wiegert, J., Liseau, R., Thébault, P., et al. 2014, A&A, 563, A102
Wittenmyer, R. A., & Marshall, J. P. 2015, AJ, 149, 86
Wright, C. O., Egan, M. P., Kraemer, K. E., & Price, S. D. 2003, AJ, 125, 359
Wright, E. L., Eisenhardt, P. R. M., Mainzer, A. K., et al. 2010, AJ, 140, 1868-1881
Wright, J. T., Marcy, G. W., Butler, R. P., & Vogt, S. S. 2004, ApJS, 152, 261
Wyatt, M. C. 2008, ARA&A, 46, 339
Wyatt, M. C., Kennedy, G., Sibthorpe, B., et al. 2012, MNRAS, 424, 1206

[1] Departmento de Astrofísica, Centro de Astrobiología (CAB, CSIC-INTA), ESAC Campus, Camino Bajo del Castillo s/n, E-28692 Villanueva de la Cañada, Madrid, Spain
[2] Universidad Autónoma de Madrid, Dpto. Física Teórica, Módulo 15, Facultad de Ciencias, Campus de Cantoblanco, E-28049 Madrid, Spain
[3] Unidad Asociada CAB–UAM
[4] Astrophysikalisches Institut und Universitätssternwarte, Friedrich-Schiller-Universität, Schillergäßchen 2-3, 07745 Jena, Germany
[5] School of Physics, UNSW Australia, Sydaney NSW 2052, Australia
[6] Australian Centre for Astrobiology, UNSW Australia, Sydney NSW 2052, Australia
[7] ESA, Directorate of Science, Scientific Support Office, European Space Research and Technology Centre (ESTEC/SCI-S), Keplerlaan 1, NL-2201 AZ Noordwijk, The Netherlands
[8] Department of Earth and Space Sciences, Chalmers University of Technology, Onsala Space Observatory, Se-439 92 Onsala, Sweden
[9] ESA-ESAC Gaia SOC, P.O. Box 78, E-28691 Villanueva de la Cañada, Madrid, Spain
[10] INAF, Osservatorio Astronomico di Palermo, Piazza Parlamento 1, 90134 Palermo, Italy
[11] Institute of Theoretical Physics and Astrophysics, Christian-Albrechts University Kiel, Leibnizstr. 15, 24118 Kiel, Germany
[12] Steward Observatory, Department of Astronomy, University of Arizona, 933 North Cherry Avenue, Tucson, AZ 85721, USA
[13] Instituto de Física y Astronomía, Facultad de Ciencias, Universidad de Valparaíso, Av. Gran Bretaña 1111, 5030 Casilla, Valparaíso, Chile
[14] ICM Nucleus on Protoplanetary Disks, Universidad de Valparaíso, Av. Gran Bretaña 1111, Valparaíso, Chile
[15] Univ. Grenoble Alpes, IPAG, F-38000 Grenoble, France
[16] CNRS, IPAG, F-38000 Grenoble, France
[17] Leiden Observatory, University of Leiden, PO Box 9513, 2300 RA, Leiden, The Netherlands
[18] NASA Goddard Space Flight Center, Exoplanets and Stellar Astrophysics, Code 667, Greenbelt, MD 20771, USA
[19] Spanish Virtual Observatory, Centro de Astrobiología (CAB, CSIC-INTA), ESAC Campus, Camino Bajo del Castillo s/n, E-28692 Villanueva de la Cañada, Madrid, Spain
[20] Instituto Nacional de Astrofísica, Óptica y Electrónica, Luis Enrique Erro 1, Santa María de Tonantzintla, Puebla, México Departamento de Astrofísica, Facultad de Ciencias Físicas, Universidad Complutense de Madrid, E-28040 Madrid

Appendix A: Rotation periods and ages

Noyes et al. (1984) studied the Ca II-Rossby number relation for several sets of mixing-length theory (MLT) models, and found out that the tightest correlation between $\log R'_{\rm HK}$ and $\mathrm{Ro} = P_{\rm rot}/\tau_{\rm c}$ was achieved for the set of models with $\alpha_{\rm MLT} = 1.9$, where $\alpha_{\rm MLT}$ is the ratio of the mixing length to the pressure scale height in the convection zone. $\tau_{\rm c}$, the turnover time, is a characteristic time of the convection whose precise definition is:

$$\tau_{\rm c} = \frac{H_{\rm p}(\mathrm{local})}{v_{\rm local}}, \tag{A.1}$$

where $H_{\rm p}$(local) is the pressure scale height and $v_{\rm local}$ is the convective velocity, both quantities computed at a distance of 0.95 $H_{\rm p}$(base cz) above the base of the outer convective zone, where $H_{\rm p}$(base cz) is the pressure scale height at the base of the convection zone.

Noyes et al. (1984) derived for that particular value of $\alpha_{\rm MLT}$ a polynomial fit for the turnover time as a function of $(B-V)$. The fit is given by the expression:

$$\log \tau_{\rm c} = \begin{cases} 1.362 - 0.166\,x + 0.025\,x^2 - 5.323\,x^3, & x > 0 \\ 1.362 - 0.14\,x, & x < 0 \end{cases} \quad \text{(A.2)}$$

where $x = 1.0 - (B-V)$ and $\tau_{\rm c}$ is given in days.

Once $\tau_{\rm c}$ has been computed, and provided $\log R'_{\rm HK}$ is known, Noyes et al. (1984) gave the following expression:

$$\log {\rm Ro} = 0.324 - 0.400\,y - 0.283\,y^2 - 1.325\,y^3 \quad \text{(A.3)}$$

which gives a direct estimation of $P_{\rm rot}$; y is defined as $y = 5.0 + \log R'_{\rm HK}$.

The determination of $P_{\rm rot}$ from the Rossby number and $\log R'_{\rm HK}$ is valid if $0.4 < (B-V) < 1.4$ and $-5.1 < \log R'_{\rm HK} < -4.3$ Quantitative similar relationships can be found in the paper by Mamajek & Hillenbrand (2008).

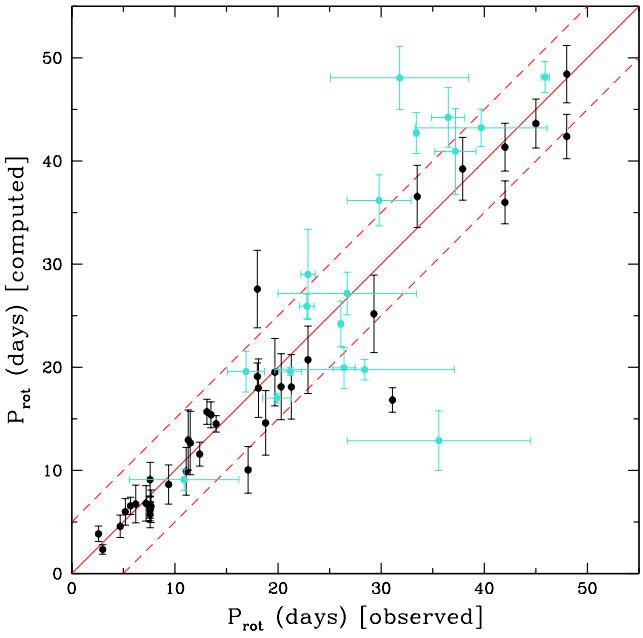

Fig. A.1. Rotation periods estimated according to the formalism described in this Appendix, plotted against the rotation periods for a sample of FGK stars with known values for $P_{\rm rot}$. Black symbols correspond to stars from Noyes et al. (1984) and cyan symbols to stars from Suárez Mascareño et al. (2015). The dashed lines mark the interval ±5 days with respect to the diagonal. See text for details.

In order to test the validity of these relationships when computing $P_{\rm rot}$ for the stars analysed in this paper, we have taken the sample of 39 FGK stars given by Noyes et al. (1984), and 19 FGK stars by Suárez Mascareño et al. (2015), plus the Sun, for which the rotation period are known by rotational modulation (first set) and time-series high-resolution spectroscopy (second set). Fig. A.1 shows the comparison between the observed rotation periods and the rotation periods estimated following the formalism described above; the Noyes et al. sample is plotted in black, the Suárez-Macareño et al. sample is plotted in light blue. The uncertainties in both (*B*–*V*) and $\log R'_{\rm HK}$ have been taken into account when available. Noyes et al. (1984) do not give any uncertainties in the observed periods nor in $\log R'_{\rm HK}$, therefore we have assumed a $\sigma(\log R'_{\rm HK}) = 0.05$. It can be seen that the agreement is fairly good, in particular for the Noyes et al. sample. Only two objects, namely HD 25171 and HD 40307, are clear outliers, therefore we can consider the values of $P_{\rm rot}$ computed for the DUNES_DB stars following this method, and shown in Table 3 as reliable.

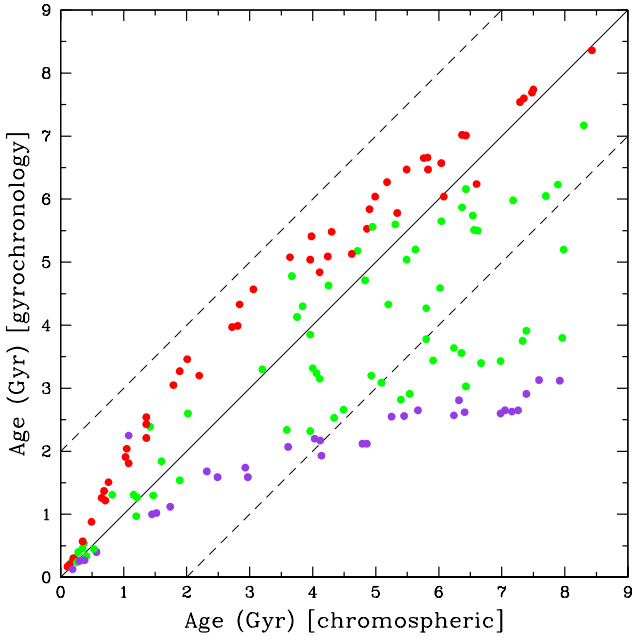

Fig. A.2. Ages for the DUNES_DU and DUNES_DB ($d \leq 20$ pc) samples estimated by gyrochronology plotted against the chromospheric ages. F, G and K stars are plotted in violet, green and red, respectively. The dashed lines mark the interval ±2 Gyr with respect to the diagonal.

Concerning the ages, all the expressions were extracted from the paper by Mamajek & Hillenbrand (2008). Assuming that $P_{\rm rot}$ is known, equations (12)–(14) with the revised gyrochronology parameters *a*, *b*, *c* and *n* in their Table 10 were used to derive the gyrochronology age (in Myr):

$$t_{\rm Gyro} = \left(\frac{P_{\rm rot}}{a\,[(B-V) - c]^b} \right)^{1/n} \quad \text{(A.4)}$$

whereas expression (A.3) was used to estimate the chromospheric age:

$$\log t_{\rm HK} = -38.053 - 17.912\,\log R'_{\rm HK} - 1.6675\,(\log R'_{\rm HK})^2 \quad \text{(A.5)}$$

where $t_{\rm HK}$ is the age in years. The gyrochronology expression is valid for $B - V > 0.495$ and the fit to estimate $t_{\rm HK}$ is only appropriate for $-5.1 < \log R'_{\rm HK} < -4.0$. Fig. A.2 shows a comparison between the ages of the whole DUNES_DU plus DUNES_DB samples estimated using both approaches; obviously only the stars for which both ages could be estimated are included in the graph. The discrepancies between the ages are clear, the differences being more pronounced for earlier spectral types.

The caveats involving the determination of ages are well known, but its detailed discussion are out of the scope of this paper (details can be found in e.g. Barnes

(2007), Mamajek & Hillenbrand (2008), Soderblom (2010), Epstein & Pinsonneault (2014), Meibom et al. (2015) and references therein). The bottom line of this analysis is that whereas the rotation periods establish a reasonable evolutionary proxy for FGK stars, in the sense that the older the star the longer the rotation period, the assignation of an specific age valid in a time span of the order of Gyr has to be taken with caution.

Appendix B: Spectral energy distributions

In this appendix the SEDs of the excess, dubious and non excess sources are shown.

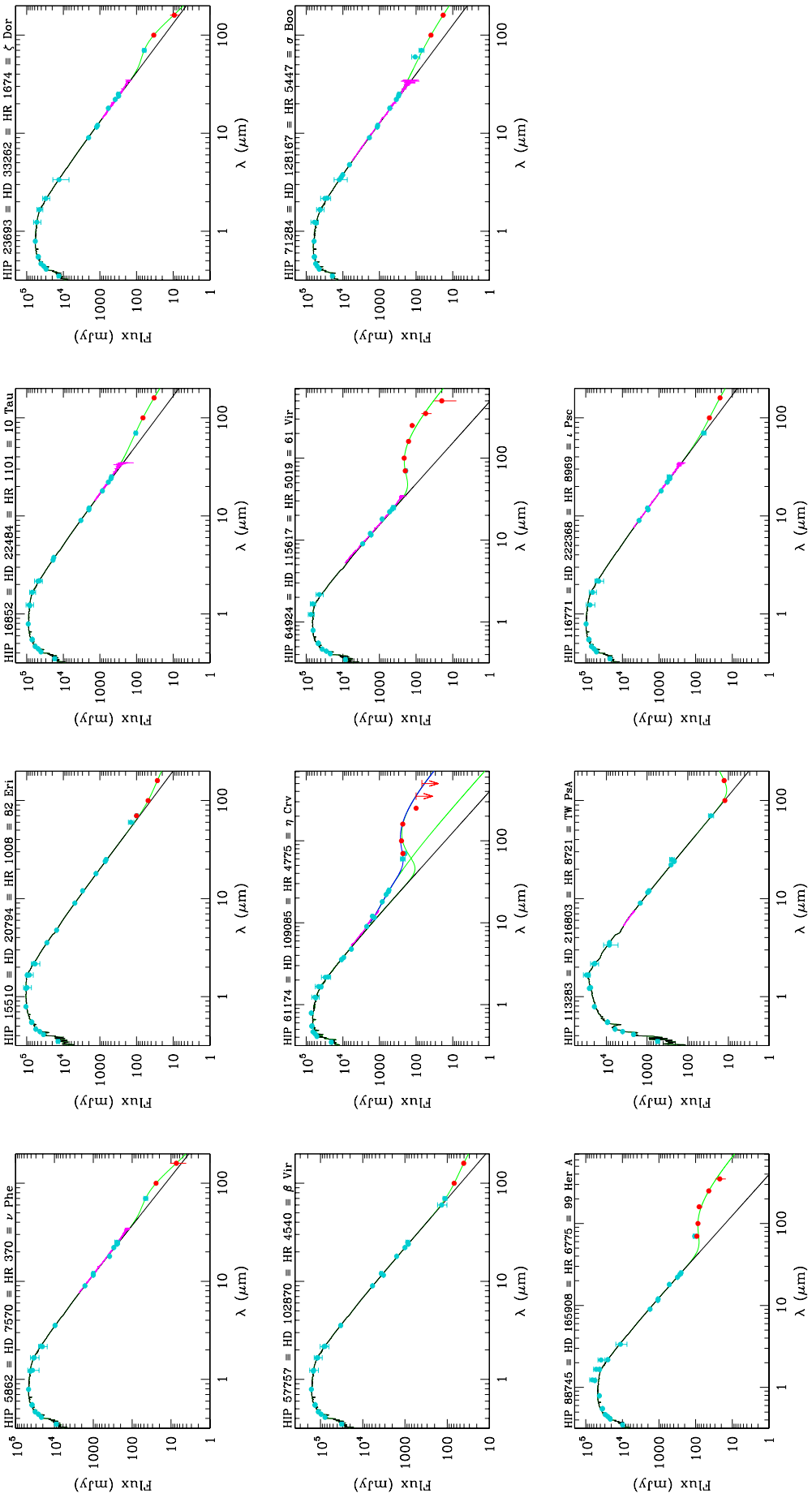

Fig. B.1. SEDs of the FGK DUNES_DB stars ($d \leq 20$ pc) with excesses.

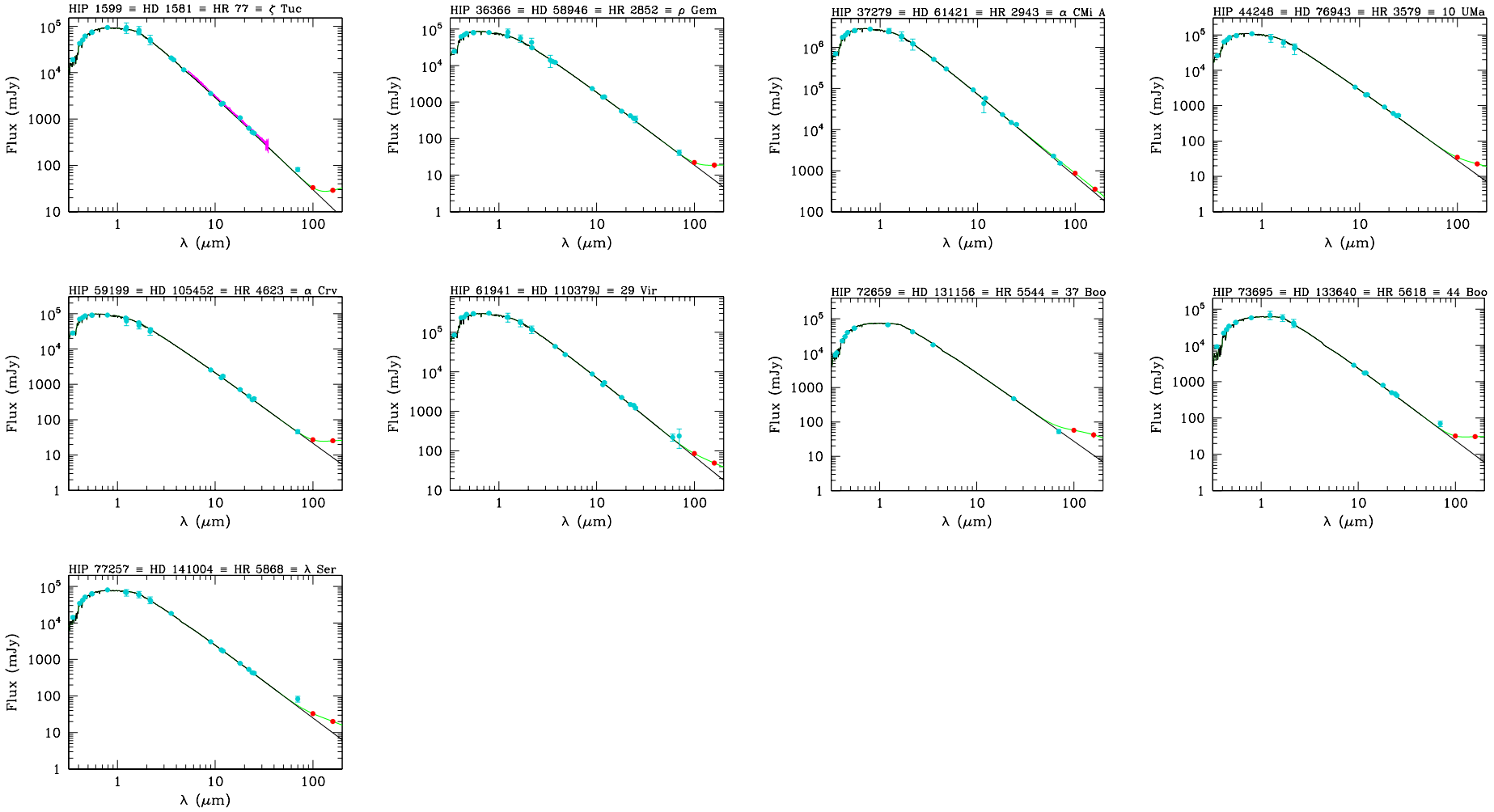

Fig. B.2. SEDs of the FGK DUNES_DB stars ($d \leq 20$ pc) showing apparent excesses but considered dubious.

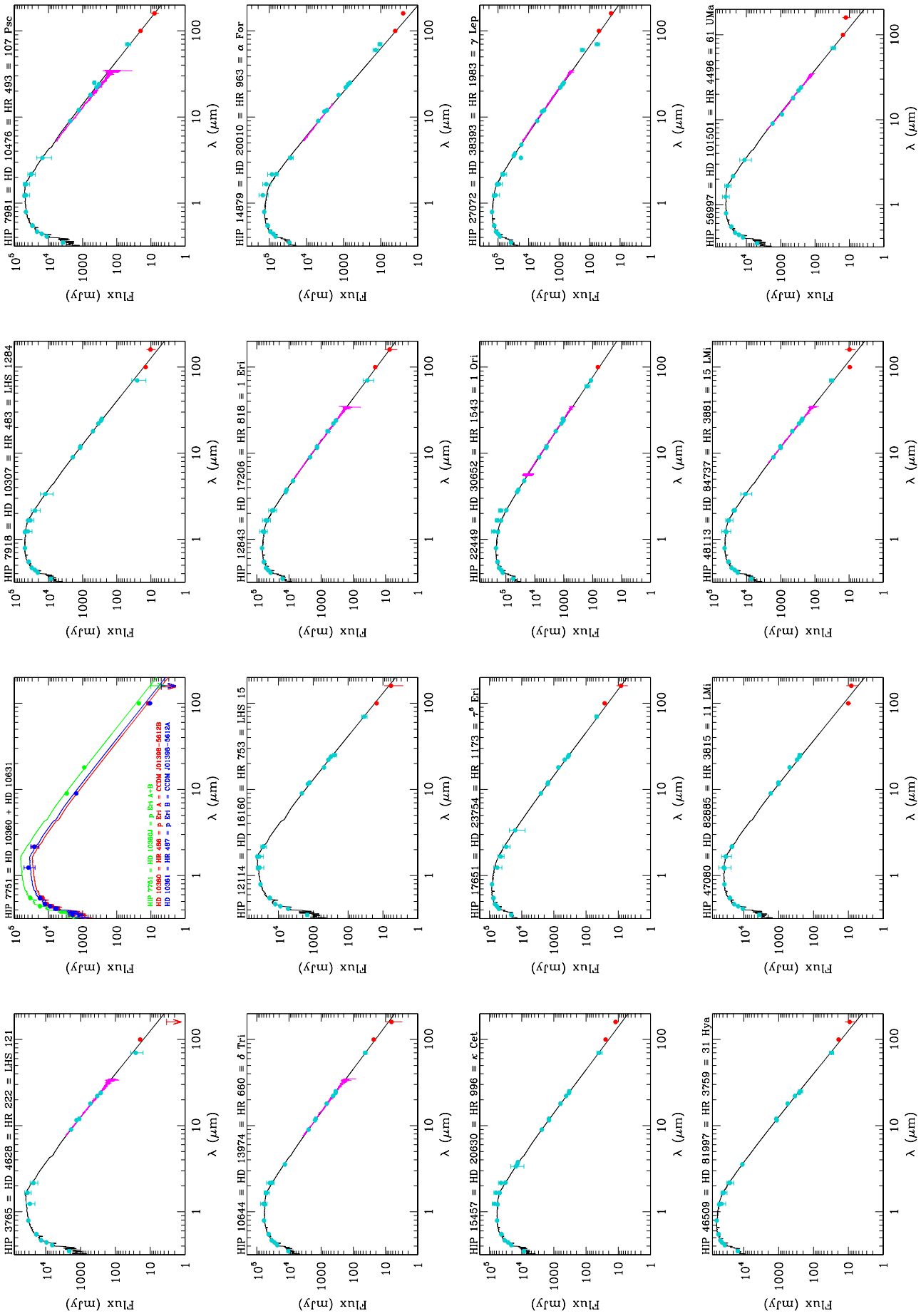

Fig. B.3. SEDs of the FGK DUNES_DB stars ($d \leq 20$ pc) without excess.

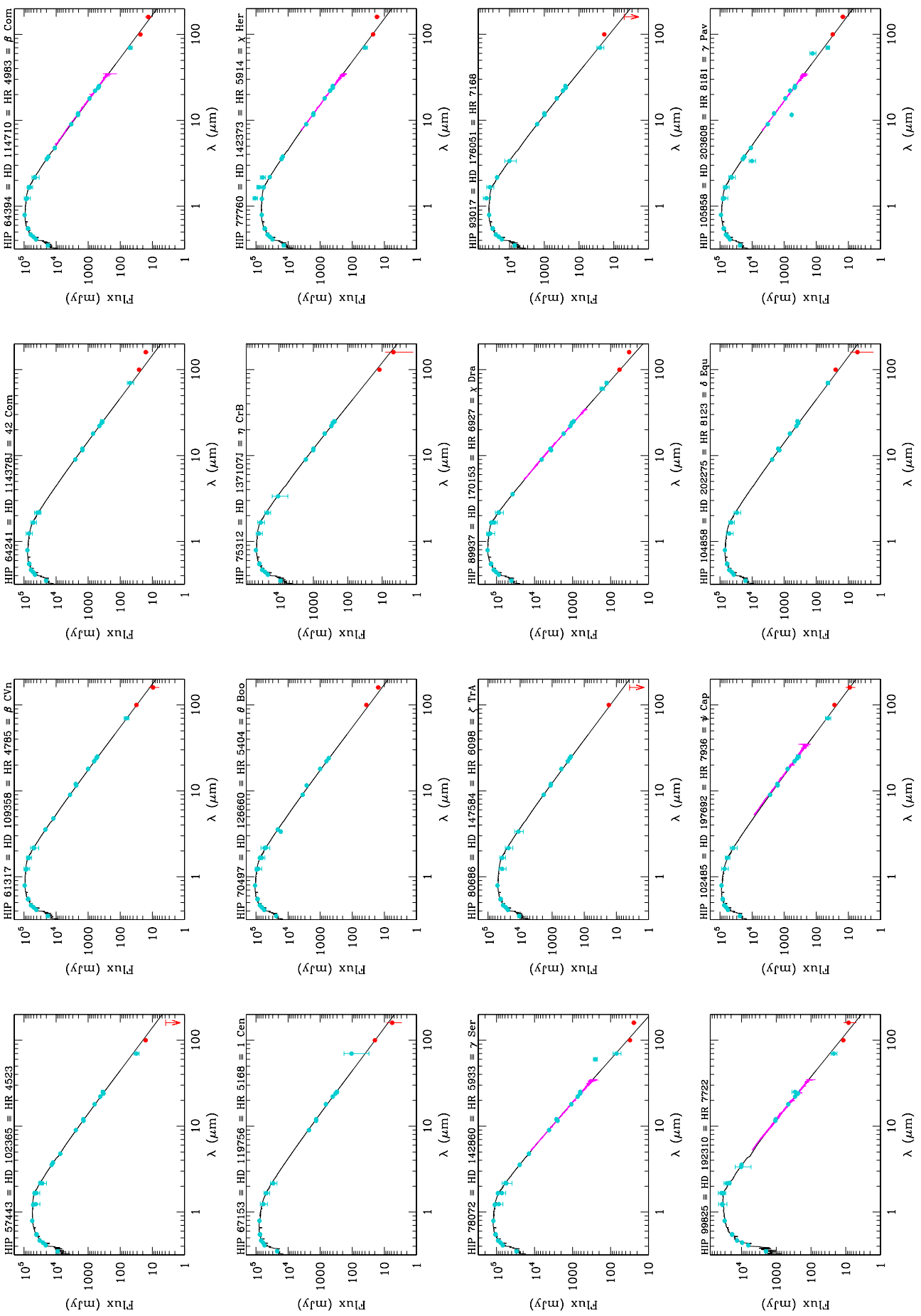

Fig. B.3. Continued.

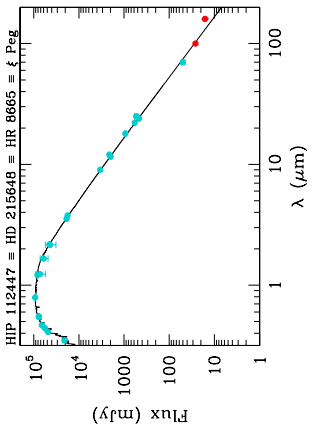

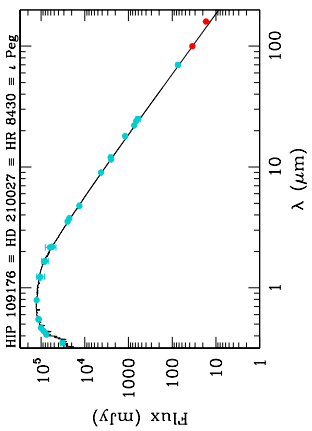

Fig. B.3. Continued.

Table 2. The subsamples of DUNES_DB with $d \leq 15$ pc and $15\,\mathrm{pc} < d \leq 20$ pc.

HIP	HD	Other ID	SpT (Hipparcos)	SpT range	ICRS (2000)		π(mas)	d(pc)
FGK stars ($d \leq 15$ pc)								
1599	1581	ζ Tuc	F9V	F9.5V, F9V–G0V	00 20 04.260	−64 52 29.25	116.46±0.16	8.59±0.01
3765	4628	LHS 121	K2V	K2.5V, K2V	00 48 22.977	+05 16 50.21	134.14±0.51	7.45±0.03
7751	10360J	p Eri	K0V	K0V, K1–K3V	01 39 47.540	−56 11 47.10	127.84±2.19	7.82±0.13
7918	10307	HR 483	G2V	G1.5V, G1V	01 41 47.143	+42 36 48.12	78.50±0.54	12.74±0.09
7981	10476	107 Psc	K1V	K1V, K0V–K1V	01 42 29.762	+20 16 06.60	132.76±0.50	7.53±0.03
10644	13974	δ Tri	G0V	G0.5V, F9V–G0V	02 17 03.230	+34 13 27.23	92.73±0.39	10.78±0.05
12114	16160	LHS 15	K3V	K3V	02 36 04.895	+06 53 12.75	139.27±0.45	7.18±0.02
12843	17206	1 Eri	F5/F6V	F6V, F5V–F8V	02 45 06.187	−18 34 21.21	70.32±1.83	14.22±0.37
14879	20010	α For	F8V	F6V, F6V–F8V	03 12 04.527	−28 59 15.43	70.24±0.45	14.24±0.09
15457	20630	κ Cet	G5Vvar	G5Vv, G5V	03 19 21.696	+03 22 12.72	109.41±0.27	9.14±0.02
15510	20794	e Eri	G8V	G8V	03 19 55.651	−43 04 11.22	165.47±0.19	6.04±0.01
16852	22484	10 Tau	F9V	F9IV-V, F9V, F9IV-V	03 36 52.383	+00 24 05.98	71.62±0.54	13.96±0.11
22449	30652	1 Ori	F6V	F6V, F6V–F6IV-V	04 49 50.411	+06 57 40.59	123.94±0.17	8.07±0.01
23693	33262	ζ Dor	F7V	F9V, F67/V–F8V	05 05 30.657	−57 28 21.74	85.87±0.18	11.65±0.02
27072	38393	γ Lep	F7V	F6.5V, F6V–F8IV	05 44 27.791	−22 26 54.18	112.02±0.18	8.93±0.01
37279	61421	α CMi A	F5IV-V	F5IV-V, F4V–F5IV-V	07 39 18.120	+05 13 29.96	284.56±1.26	3.51±0.02
47080	82885	11 LMi	G8IV-V	G8IIIv, G8V–G8IV	09 35 39.503	+35 48 36.49	87.96±0.32	11.37±0.04
56997	101501	61 UMa	G8Vvar	G8V	11 41 03.016	+34 12 05.88	104.04±0.26	9.61±0.02
57443	102365	LHS 311	G3/G5V	G2V,G2.5III, G5V	11 46 31.073	−40 30 01.27	108.45±0.22	9.22±0.02
57757	102870	β Vir	F8V	F9V, F8.5IV-V	11 50 41.718	+01 45 52.99	91.50±0.22	10.93±0.03
59199	105452	α Crv	F0IV/V	F1V, F0IV-V, F2III-IV, F2V	12 08 24.817	−24 43 43.95	66.95±0.15	14.94±0.03
61317	109358	β CVn	G0V	G0V	12 33 44.545	+41 21 26.92	118.49±0.20	8.44±0.01
61941	110379J	29 Vir	F0V+...	F0V, A7V–F2V	12 41 39.643	−01 26 57.74	85.58±0.60	11.68±0.08
64394	114710	β Com	G0V	G0V, F8/9V–G0V	13 11 52.394	+27 52 41.45	109.54±0.17	9.13±0.01
64924	115617	61 Vir	G5V	G7V, G6.5V	13 18 24.314	−18 18 40.30	116.89±0.22	8.56±0.02
70497	126660	θ Boo	F7V	F7V, F7II–III	14 25 11.797	+51 51 02.68	68.82±0.14	14.53±0.03
72659	131156	37 Boo	G8V + K4V	G8V, G7V–G8V	14 51 23.380	+19 06 01.70	148.98±0.48	6.71±0.02
73695	133640	44 Boo	G2V + G2V	G0Vnv, F5V–G2V	15 03 47.296	+47 39 14.62	79.95±1.56	12.51±0.24
77257	141004	λ Ser	G0Vvar	G0V, G0IV-V–G0V	15 46 26.614	+07 21 11.04	82.48±0.32	12.12±0.05
78072	142860	γ Ser	F6V	F6IV, F6V–F7V	15 56 27.183	+15 39 41.82	88.86±0.18	11.25±0.02
80686	147584	ζ TrA	F9V	F9V, F6(V)+G1?(V)	16 28 28.144	−70 05 03.84	82.53±0.52	12.12±0.08
89937	170153	χ Dra	F7Vvar	F7V, F7V–F8V	18 21 03.383	+72 43 58.25	124.11±0.87	8.06±0.06
93017	176051	HR 7162	G0V	F9V, F9V–G0V	18 57 01.610	+32 54 04.57	67.24±0.37	14.87±0.08
99825	192310	HR 7722	K3V	K2+v, K2V	20 15 17.391	−27 01 58.71	112.22±0.30	8.91±0.02
102485	197692	ψ Cap	F5V	F5V, F4V–F6V	20 46 05.733	−25 16 15.23	68.13±0.27	14.68±0.06
105858	203608	γ Pav	F6V	F9V, F6V–F8V	21 26 26.605	−65 21 58.31	107.97±0.19	9.26±0.02
109176	210027	ι Peg	F5V	F5V, F5V–F6V	22 07 00.666	+25 20 42.40	85.28±0.63	11.73±0.09
113283	216803	TW PsA	K4Vp	K4+vk, K3V–K5V	22 56 24.053	−31 33 56.04	131.42±0.62	7.61±0.04
116771	222368	ι Psc	F7V	F7V, F7V–F8V	23 39 57.041	+05 37 34.65	72.92±0.15	13.71±0.03
FGK stars ($15\,\mathrm{pc} < d \leq 20$ pc)								
5862	7570	ν Phe	F8V	F9V, F9V	01 15 11.121	−45 31 54.00	66.16±0.24	15.11±0.05
17651	23754	27 Eri	F3/F5V	F5IV-V, F3III	03 46 50.888	−23 14 59.00	56.73±0.19	17.63±0.06
36366	58946	ρ Gem	F0V...	F0V, F0V–F3V	07 29 06.719	+31 47 04.38	55.41±0.24	18.05±0.08
44248	76943	10 UMa	F5V	F5V, F5V–F7V	09 00 38.381	+41 46 58.61	62.23±0.68	16.07±0.18
46509	81997	31 Hya	F6V	F6V, F5.5IV-V–F6IV-V	09 29 08.897	−02 46 08.26	57.69±2.14	17.33±0.64
48113	84737	15 LMi	G2V	G0.5Va, G0IV-V	09 48 35.371	+46 01 15.63	54.44±0.28	18.37±0.09
61174	109085	η Crv	F2V	F2V, F0III, FOIV, F2III	12 32 04.227	−16 11 45.62	54.70±0.17	18.28±0.06
64241	114378J	42 Com	F5V	F5V, F5.5V–F7V	13 09 59.285	+17 31 46.04	56.10±0.89	17.83±0.28
67153	119756	i Cen	F3V	F2V, F3IV, F2V	13 45 41.245	−33 02 37.40	51.54±0.19	19.40±0.07
71284	128167	σ Boo	F3Vwvar	F2V, F3V–F5V	14 34 40.817	+29 44 42.46	63.16±0.25	15.83±0.06
75312	137107J	η CrB	G2V	G2V, F9V–G2V	15 23 12.305	+30 17 16.17	55.98±0.78	17.86±0.25
77760	142373	χ Her	F9V	F8Ve..., F8V–G0V	15 52 40.541	+42 27 05.47	62.92±0.21	15.89±0.05
88745	165908	99 Her A	F7V	F7V, F7V–F9V	18 07 01.540	+30 33 43.69	63.93±0.34	15.64±0.08
104858	202275	δ Equ	F5V+...	F5V+..., F7V–G1V	21 14 28.815	+10 00 25.13	54.09±0.66	18.49±0.23
112447	215648	ξ Peg	F7V	F7V, F5V–F7V	22 46 41.581	+12 10 22.39	61.36±0.19	16.30±0.05

Table 3. Parameters of the DUNES_DB stars with $d \leq 15$ pc and $15\,\mathrm{pc} < d \leq 20$ pc.

HIP	$T_{\rm eff}$ (K)	$\log g$ (cm/s^2)	[Fe/H] (dex)	Flag	$L_{\rm bol}$ ($L_\odot$)	$\log R'_{\rm HK}$	Ref	$P_{\rm rot}$ (d) or lower limit†	$t_{\rm Gyro)}$ (Gyr)	$t_{\rm HK}$ (Gyr)
FGK stars ($d \leq 15$ pc)										
1599	5960	4.45	−0.17	S	1.224	−4.855	1	14.01 ± 0.97	2.20	4.03
3765	4977	4.57	−0.22	S	0.283	−4.852	2	39.02 ± 0.25	5.41	3.98
7751	4993	4.54	−0.23	S	0.304	−4.94	3			
7918	5891	4.36	+0.06	S	1.405	−4.987	4	21.10 ± 0.12	3.56	6.36
7981	5189	4.52	−0.04	S	0.439	−4.912	2	39.60 ± 0.43	6.04	4.99
10644	5684	4.36	−0.45	P	1.118	−4.644	4	11.57 ± 0.35	1.30	1.47
12114	4866	4.66	+0.00	S	0.257	−4.958	2	44.90 ± 0.53	6.66	5.82
12843	6273	4.20	−0.04	P	2.585	−4.524	1	2.92 ± 0.36		0.71
14879	6275	4.40	−0.19	S	4.923	−4.901	1	11.58 ± 1.39	2.12	4.79
15457	5755	4.52	+0.11	S	0.838	−4.42	2	7.53 ± 0.18	0.46	0.35
15510	5415	4.55	−0.34	S	0.637	−4.998	1	32.42 ± 0.55	5.51	6.56
16852	6014	4.08	−0.06	S	3.060	−5.053	4	17.06 ± 0.95	3.13	7.59
22449	6457	4.15	−0.01	S	2.708	−4.788	4	5.83 ± 0.18		3.04
23693	6165	4.38	−0.20	P	1.414	−4.49	3	3.91 ± 0.37	0.40	0.57
27072	6331	4.28	−0.10	P	2.291	−4.817	1	5.91 ± 0.66		3.45
37279	6578	3.99	+0.01	S	6.605	−4.777	2	3.21 ± 0.59		2.89
47080	5539	4.48	+0.33	S	0.822	−4.638	2	21.86 ± 0.10	2.39	1.42
56997	5514	4.50	−0.04	S	0.618	−4.546	2	14.62 ± 0.65	1.31	0.82
57443	5630	4.51	−0.28	S	0.806	−4.957	1	25.90 ± 0.47	4.27	5.80
57757	6125	4.12	+0.14	S	3.483	−4.99	5	10.27 ± 1.37	2.62	6.41
59199	7042	4.21	−0.14	P	4.175	−5.373	6	> 3.26 (21.7)		
61317	5890	4.40	−0.17	S	1.178	−4.851	4	15.11 ± 0.89	2.32	3.96
61941	6797	4.25	−0.13	P	8.346	−4.50	6	6.31 ± 0.37‡		0.61
64394	6065	4.43	+0.04	S	1.381	−4.745	2	11.48 ± 0.49	1.59	2.49
64924	5646	4.57	+0.10	S	0.820	−5.001	2	32.29 ± 0.78	5.50	6.62
70497	6315	4.29	−0.10	P	4.034	−4.591	4	4.26 ± 0.21	2.25	1.08
72659	5549	4.63	−0.10	S	0.611	−4.363	2	6.49 ± 0.31	0.31	0.23
73695	5851	4.30	−0.19	S	1.552	−4.602	4	12.85 ± 0.13	1.31	1.16
77257	5899	4.17	+0.01	S	2.077	−5.004	2	19.73 ± 0.96	3.40	6.67
78072	6265	4.08	−0.15	S	2.863	−5.113	4	> 5.2 (11.42)		
80686	6029	4.46	−0.19	P	1.301	−4.65	3	8.25 ± 1.00	1.02	1.52
89937	6034	4.27	−0.65	P	1.942	−4.9	6	7.13 ± 0.35		4.78
93017	5834	4.33	−0.19	P	1.515	−4.874	2	16.18 ± 0.31	2.53	4.34
99825	5105	4.48	−0.03	S	0.405	−5.048	1	47.33 ± 0.78	7.74	7.50
102485	6590	4.26	−0.05	P	3.705	−4.404	1	0.94 ± 0.06		0.31
105858	6089	4.38	−0.68	P	1.400	−4.491	1	2.93 ± 0.57		0.57
109176	6448	4.25	0.12	P	3.303	−5.06	7	4.61 ± 0.39		7.72
113283	4555	4.53	−0.01	S	0.181	−4.467	1	16.03 ± 0.03	0.88	0.49
116771	6180	4.09	−0.10	S	3.319	−5.112	4	> 8.58 (6.67)	> 2.27	
FGK stars ($15\,\mathrm{pc} < d \leq 20$ pc)										
5862	6128	4.36	+0.16	S	1.913	−4.861	1	13.63 ± 0.68	2.17	4.12
17651	6654	4.11	+0.09	P	4.930	−4.684	1	2.74 ± 0.40		1.83
36366	7086	4.13	−0.25	P	5.351	−4.66	6	2.50 ± 0.36‡		1.61
44248	6556	4.01	+0.04	P	5.249	−4.548	8	2.62 ± 0.09		0.83
46509	6486	4.22	−0.01	P	3.369	−4.828	4	2.66 ± 0.52		3.61
48113	5940	4.05	+0.14	S	2.618	−5.042	4	22.30 ± 0.89	3.91	7.39
61174	6784	4.06	−0.05	P	4.873	−5.173	6	> 1.12 (59.15)		
64241	6376	4.26	−0.21	P	4.625	−4.53	2	2.26 ± 0.20		0.74
67153	6745	3.88	−0.09	P	5.857	−4.56	6	2.42 ± 0.22‡		0.90
71284	6727	4.32	−0.35	S	3.112	−5.476	4	> 9.34 (7.32)		
75312	5949	4.15	−0.06	S	2.631	−4.828	2	13.60 ± 0.38	2.07	3.61
77760	5840	3.94	−0.49	S	2.962	−5.042	2	15.50 ± 1.59	2.91	7.39
88745	6089	4.18	−0.53	S	1.867	−5.02	9	11.52 ± 0.20	2.60	6.98
104858	6250	4.40	−0.07	P	4.450	−4.905	8	10.36 ± 1.32	2.12	4.86
112447	6181	3.93	−0.24	S	4.387	−5.276	4	> 4.55 (12.67)	> 1.23	

Notes: $T_{\rm eff}$, $\log g$ and [Fe/H] are averages from Fuhrmann (2008), Gray et al. (2003), Gray et al. (2006), Holmberg et al. (2009), Santos et al. (2004), Sousa et al. (2008), Takeda et al. (2005) and Valenti & Fischer (2005).
'S' and 'P' in col. 5 mean that the determination is spectroscopic or photometric.
$\log g$ for HIP 104858 assigned according to its spectral type.
References for $\log R'_{\rm HK}$: (1) Gray et al. (2006), (2) Baliunas et al. (1996), (3) Martínez-Arnáiz et al. (2010), (4) Duncan et al. (1991), (5) Hall et al. (2007), (6) $R'_{\rm HK}$ computed from ROSAT X-ray data using eqn. A1 from Mamajek & Hillenbrand (2008), (7) Saffe et al. (2005), (8) Gray et al. (2003), (9) Wright et al. (2004).
Determination of $P_{\rm rot}$ from the Rossby number and $\log R'_{\rm HK}$ valid if $0.4 < B-V < 1.4$ and $-5.1 < \log R'_{\rm HK} < -4.3$ (Noyes et al. 1984).
†: When a lower limit of the period is given, the number in parentheses is the value of $v \sin i$ (km/s) used to estimate it.
‡: The $(B-V)$ value is slighly ouside the valid range of the Noyes et al. (1984) calibratio for$P_{\rm rot}$.
Gyrochronology age calibration valid if $B-V > 0.5$ (Mamajek & Hillenbrand 2008).
Chromospheric age calibration valid in the interval $-5.0 < \log R'_{\rm HK} < -4.3$ (Mamajek & Hillenbrand 2008).

Table 4. Multiplicity and planetary companions of the DUNES_DB stars with $d < 20$ pc.

HIP	Multiplicity and details	CCDM identification	ICRS (2000) α (hh mm ss)	δ (deg min sec)	$\mu_\alpha \cos(\delta)$ (mas/yr)	μ_δ (mas/yr)	Separation (arcsec)
FGK stars ($d \leq 15$ pc)							
7751	Double or multiple star						
	p Eri B K2V V=5.797	CCDM J01398-5612A	01 39 47.557	−56 11 47.34	286.10	16.16	11.18
	p Eri A K2V V=5.96	CCDM J01398-5612B	01 39 47.555	−56 11 36.16	286.10	16.16	
7918	Spectroscopic binary						
10644	Spectroscopic binary	CCDM J02170+3414A					
12843	Spectroscopic binary						
14879	Double or multiple star						
	α For A, F6V, V=3.98	CCDM J03121-2859A	03 12 04.294	−28 59 20.42	371.49	612.26	7.50
	α For B, G7V, V=7.1	CCDM J03121-2859B	03 12 04.211	−28 59 13.00	345.78	648.31	
37279	Spectroscopic binary						
	α CMi A, F5IV-V, V=0.37	CCDM J07393+0514A	07 39 18.118	+05 13 29.97			0.27
	α CMi B, DQZ, V=10.92	CCDM J07393+0514B	07 39 18.1	+05 13 30			
47080	Variable of RS CVn type						
	11 LMi A, G8+V, V=5.48	CCDM J09357+3549A	09 35 39.506	+35 48 36.75			6.11
	11 LMi B, M5V, V=13.0	CCDM J09357+3549B	09 35 39.97	+35 48 39.1			
61317	Spectroscopic binary	CCDM J12337+4121AB					
61941	Double or multiple star						
	γ Vir A, F0IV, V=3.440	CCDM J12417-0127A	12 41 39.983	−01 26 58.25	−616.66	+60.66	2.62
	γ Vir B, F0IV, V=3.484	CCDM J12417-0127B	12 41 39.813	−01 26 57.63	−523.91	−39.05	
72659	Variable of BY Dra type						
	ξ Boo A, G7Ve, V=4.675	CCDM J14513+1906A	14 51 23.286	+19 06 02.25	152.81	−71.28	
	ξ Boo B, K5Ve, V=6.816	CCDM J14513+1906B			89.72	−147.30	
73695	Eclipsing binary of W UMa type (contact binary)						
	i Boo A, F5V, V=5.136	CCDM J15038+4739A	15 03 47.301	+47 39 14.55	−436.24	18.94	2.31
	i Boo B, G9:, V=6.004	CCDM J15038+4739B	15 03 47.484	+47 39 15.93	−378.67	40.02	
77257	Spectroscopic binary						
80686	Spectroscopic binary						
89937	Spectroscopic binary	CCDM J18211+7245A					
93017	Spectroscopic binary						
	HD 176051A, F9V, V=5.277	CCDM J18570+3254A	18 57 01.470	+32 54 05.77	202.85	−143.97	0.99
	HD 176051B, K1V, V 7.84	CCDM J18570+3254B	18 57 01.493	+32 54 06.72	124.14	−137.92	
109176	Spectroscopic binary	CCDM J22070+2520A					
FGK stars (15 pc $< d \leq 20$ pc)							
36366	Double or multiple star						
	ρ Gem, F1V, V=4.18	CCDM J07290+3147AB	07 29 06.71887	+31 47 04.3773			12.42
	ρ Gem B, M5 D, V=12.5	CCDM J07290+3147B	07 29 06.0	+31 46 56			
44248	Spectroscopic binary						
	10 UMa A, F3V, V=4.14	CCDM J09007+4147A	09 00 38.38	+41 46 58.6	−487.67	−219.29	0.00
	10 UMa B, G5V, V=5.97	CCDM J09007+4147B	09 00 38.38	+41 46 58.6	−381.62	−270.08	
46509	Spectroscopic binary						
	τ^{01} Hya, F6V, V=4.60	CCDM J09291-0246A	09 29 08.89655	−02 46 08.2649			65.56
	τ^{01} Hya B, K0 D, V=7.15	CCDM J09291-0246B	09 29 09.2290	−02 45 02.897			
64241	Double or multiple star						
	α Com A, F5V, V=4.85	CCDM J13100+1732A	13 09 59.28	+17 31 45.86			0.38
	α Com B, F6V, V=5.53	CCDM J13100+1732B	13 09 59.28	+17 31 46.24			
67153	Spectroscopic binary						
75312	Spectroscopic binary						
	η CrB A, G2V, V=5.577	CCDM J15233+3018A	15 23 12.23	+30 17 17.56	125.77	−176.48	1.03
	η CrB B, G2V, V=5.95	CCDM J15233+3018B	15 23 12.27	+30 17 18.46	169.99	−204.58	
88745	Double or multiple star						
	b Her A, F7V, V=5.13	CCDM J18071+3034A	18 07 01.60	+30 33 42.77	−100.93	111.70	1.27
	b Her B, K4V, V=8.96	CCDM J18071+3034B	18 07 01.59	+30 33 44.03	−69.00	48.08	
104858	Spectroscopic binary	CCDM J21145+1001AB			42.32	−303.43	

HIP	Comment	CCDM identification	Planets		
				M/M_{Jup}	a (UA)
15510	High proper-motion star		b	0.009	0.12
			c	0.008	0.20
			d	0.015	0.35
57443	High proper-motion star	CCDM J11465-4030A	b	0.05	0.46
64924	High proper-motion star	CCDM J13185-1818A	b	0.016	0.05
			c	0.057	0.22
			d	0.072	0.48
93017	Spectroscopic binary		b	1.5	1.76
99825	Variable star		b	0.053	0.32
			c	0.076	1.18

All planets discovered by the radial velocity (RV) method except HIP 93017b (astrometry), therefore masses for the RV exoplanets are lower limits.
Data from http://exoplanetarchive.ipac.caltech.edu/docs/data.html except for HIP 93017b, which are taken from http://exoplanet.eu

Table 5a. Johnson V, $B-V$, Cousins $V-I$ and Strömgren photometry.

HIP	V (mag)	$B-V$ (mag)	$V-I$ (mag)	$b-y$ (mag)	m_1 (mag)	c_1 (mag)
FGK stars ($d \leq 15$ pc)						
1599	4.23	0.576±0.010	0.65±0.02	0.368±0.003	0.177±0.004	0.302±0.020
3765	5.74	0.890±0.008	0.97±0.02	0.512±0.003	0.423±0.002	0.255±0.004
7751	5.76	0.880±0.400	0.93±0.02	0.512	0.421	0.262
7918	4.96	0.618±0.001	0.67±0.03	0.389±0.000	0.198±0.005	0.348±0.011
7981	5.24	0.836±0.008	0.88±0.01	0.492±0.002	0.367±0.007	0.296±0.006
10644	4.84	0.607±0.005	0.76±0.07	0.390±0.003	0.186±0.003	0.259±0.004
12114	5.79	0.918±0.019	1.06±0.02	0.555±0.003	0.517±0.002	0.273±0.006
12843	4.47	0.481±0.012	0.54±0.02	0.328	0.167	0.406
14879	3.80	0.543±0.015	0.63±0.02	0.339	0.156	0.411
15457	4.84	0.681±0.006	0.73±0.02	0.419±0.003	0.235±0.005	0.307±0.003
15510	4.26	0.711±0.005	0.79±0.02	0.440±0.004	0.229±0.005	0.295±0.009
16852	4.29	0.575±0.008	0.66±0.02	0.367±0.003	0.173±0.004	0.376±0.004
22449	3.19	0.484±0.003	0.53±0.02	0.298±0.002	0.163±0.002	0.415±0.004
23693	4.71	0.526±0.011	0.60±0.00	0.338±0.002	0.167±0.004	0.328±0.006
27072	3.59	0.481±0.011	0.57±0.02	0.314±0.004	0.162±0.007	0.392±0.008
37279	0.40	0.432±0.015	0.49±0.02	0.272±0.000	0.167±0.000	0.532±0.000
47080	5.40	0.770±0.002	0.78±0.01	0.473±0.002	0.307±0.006	0.370±0.004
56997	5.31	0.723±0.014	0.78±0.04	0.444±0.000	0.271±0.005	0.291±0.004
57443	4.89	0.664±0.004	0.73±0.02	0.410±0.004	0.208±0.004	0.278±0.001
57757	3.59	0.518±0.015	0.61±0.02	0.354±0.003	0.187±0.003	0.416±0.009
59199	4.02	0.334±0.015	0.40±0.02	0.213±0.004	0.163±0.006	0.577±0.007
61317	4.24	0.588±0.009	0.67±0.01	0.385±0.000	0.182±0.001	0.298±0.006
61941	2.74	0.368±0.017	0.43±0.02	0.195	0.168	0.714
64394	4.23	0.572±0.006	0.67±0.04	0.368±0.002	0.192±0.002	0.338±0.003
64924	4.74	0.709±0.007	0.75±0.02	0.433±0.001	0.255±0.002	0.325±0.005
70497	4.04	0.497±0.005	0.59±0.12	0.334	0.156	0.418
72659	4.54	0.720±0.015	0.82±0.03	0.449	0.263	0.255
73695	4.83	0.647±0.002	0.71±0.00	0.420±0.002	0.202±0.004	0.289±0.006
77257	4.42	0.604±0.008	0.66±0.02	0.383±0.003	0.192±0.003	0.364±0.004
78072	3.85	0.478±0.006	0.54±0.02	0.319±0.003	0.150±0.002	0.401±0.002
80686	4.90	0.555±0.016	0.64±0.02	0.351±0.006	0.175±0.003	0.321±0.007
89937	3.55	0.489±0.005	0.62±0.04	0.336±0.002	0.145±0.004	0.320±0.012
93017	5.20	0.594±0.003	0.66±0.00	0.387±0.001	0.188±0.000	0.319±0.002
99825	5.73	0.878±0.018	0.93±0.02	0.516±0.005	0.442±0.001	0.292±0.003
102485	4.13	0.426±0.005	0.49±0.02	0.276±0.002	0.163±0.004	0.466±0.007
105858	4.21	0.494±0.020	0.61±0.02	0.331±0.004	0.124±0.004	0.313±0.007
109176	3.77	0.435±0.007	0.51±0.03	0.294±0.005	0.161±0.004	0.446±0.001
113283	6.48	1.094±0.006	1.20±0.02	0.631±0.007	0.648±0.016	0.175±0.002
116771	4.13	0.507±0.006	0.59±0.02	0.330±0.002	0.163±0.004	0.399±0.003
FGK stars (15 pc $< d \leq$ 20 pc)						
5862	4.97	0.571±0.007	0.62±0.02	0.364±0.004	0.180±0.005	0.393±0.008
17651	4.22	0.434±0.012	0.51±0.02	0.281±0.002	0.166±0.003	0.488±0.005
36366	4.16	0.320±0.012	0.40±0.03	0.215±0.000	0.155±0.001	0.615±0.001
44248	3.96	0.463±0.003	0.53±0.00	0.286	0.173	0.499
46509	4.59	0.411±0.015	0.52±0.02	0.296±0.001	0.164±0.002	0.451±0.003
48113	5.08	0.619±0.007	0.68±0.03	0.389±0.001	0.203±0.001	0.383±0.003
61174	4.30	0.388±0.014	0.44±0.02	0.244±0.003	0.167±0.006	0.543±0.006
64241	4.32	0.455±0.008	0.53±0.01	0.304±0.005	0.151±0.005	0.389±0.016
67153	4.23	0.390±0.017	0.44±0.02	0.246±0.002	0.163±0.005	0.550±0.007
71284	4.47	0.364±0.005	0.41±0.03	0.254±0.003	0.134±0.004	0.480±0.005
75312	4.99	0.577±0.004	0.65±0.00	0.367±0.002	0.186±0.001	0.338±0.003
77760	4.60	0.563±0.014	0.63±0.02	0.381±0.001	0.146±0.005	0.328±0.004
88745	5.05	0.528±0.002	0.60±0.00	0.356±0.002	0.135±0.003	0.322±0.005
104858	4.47	0.529±0.015	0.57±0.02	0.330±0.003	0.162±0.005	0.401±0.015
112447	4.20	0.502±0.007	0.60±0.03	0.331±0.002	0.147±0.002	0.407±0.001

Notes: Johnson *BV* and Cousins *I* magnitudes are from the *Hipparcos* catalogue (I/239 in Vizier); the calibration from magnitudes to fluxes is carried out using the zero points by Bessell (1979). Strömgren $b-y$, m_1 and c_1 are taken from Hauck & Mermilliod (1997) (catalogue II/215 in Vizier) and Hauck & Mermilliod (1998); these indices were converted into *uvby* magnitudes, and then into fluxes using the zero points by Gray (1998).

Table 5b. 2MASS JHK_s and ancillary Johnson $JHKLL'M$ photometry.

HIP	2MASS J (mag)	2MASS H (mag)	2MASS K_s (mag)	Qflag	J (mag)	H (mag)	K (mag)	L (mag)	L' (mag)	M (mag)	Refs.
FGK stars ($d \leq 15$ pc)											
1599	3.068±0.272	2.738±0.218	2.769±0.250	DDD	3.196	2.880	2.832	2.803	2.795	2.856	1,2,3
3765	4.367±0.310	3.722±0.230	3.683±0.268	DDD							
7751A			3.558±0.270	D							
7751B	4.043±0.378		3.510±0.282	D D							
7918	4.000±0.262	3.703±0.226	3.577±0.314	DDD	3.800	3.560					2
7981	3.855±0.240	3.391±0.226	3.285±0.266	DDD	3.775	3.345	3.285				2
10644	3.525±0.246	3.287±0.206	3.076±0.276	DCD	3.643	3.284	3.235	3.290			2,4
12114	4.152±0.264	3.657±0.244	3.481±0.208	DDC	4.068	3.543	3.457				2
12843	3.486±0.292	3.236±0.306	3.249±0.296	DDD	3.607	3.380	3.339	3.350	3.308	3.328	2,3,5,6
14879	2.572±0.292	2.317±0.268	2.238±0.332	DDD			2.510				2
15457	3.407±0.192	3.039±0.182	2.957±0.212	CCC	3.668	3.353	3.288	3.259	3.190		2,6,7
15510	3.032±0.262	2.709±0.234	2.636±0.278	DDD	2.993	2.591	2.551	2.490		2.560	1,3
16852	3.194±0.246	2.916±0.200	2.835±0.260	DCD	3.247		2.911	2.905	2.840		2,6,7
22449	1.984±0.246	1.757±0.132	1.600±0.196	DBC	2.349	2.139	2.080	2.068	2.069	2.093	2,3,5,6,8,9
23693	3.701±0.248	3.407±0.202	3.371±0.234	DCD							
27072	2.804±0.276	2.606±0.236	2.508±0.228	DDD	2.696	2.462	2.410	2.390	2.367	2.421	1,2,3,6,8
37279	–0.498±0.151	–0.666±0.270	–0.658±0.322	BDD	–0.420	–0.576	–0.664	–0.670		–0.670	2,3,6,9
47080	4.059±0.410	3.718±0.338	3.690±0.018	DDE	4.140	3.770	3.700				2
56997	3.988±0.242	3.648±0.228	3.588±0.036	DDE							
57443	3.931±0.276	3.490±0.238	3.489±0.278	DDD	3.745	3.377	3.312	3.261	3.246	3.341	1,2,3,6
57757	2.597±0.252	2.363±0.230	2.269±0.254	DDD	2.602	2.347	2.316	2.300			2,5,6
59199	3.525±0.286	3.364±0.218	3.307±0.240	DDD	3.337	3.195	3.165				2
61317	3.213±0.218	2.905±0.198	2.848±0.310	DCD	3.195	2.900	2.813	2.770		2.800	2,6
61941	2.041±0.272	1.925±0.224	1.873±0.232	DDD	2.081	1.922	1.876		1.880	1.917	2
64394	3.232±0.234	2.992±0.192	2.923±0.274	DCD	3.204	2.918	2.878	2.870	2.880	2.908	2,4,6,8,9
64924	3.334±0.200	2.974±0.176	2.956±0.236	CCD							
70497	3.179±0.244	2.980±0.216	2.739±0.332	DCD	3.087	2.853	2.820	2.803			2,5,6
72659	2.660±0.448	2.253±0.698	1.971±0.600	DDD	3.984	3.000	3.395	3.479	3.715		2,7
73695	3.416±0.282	3.125±0.228	3.011±0.268	DDD			3.100				2
77257	3.430±0.220	3.070±0.216	2.989±0.230	DCD	3.434	3.122	3.043	2.950			2,6
78072	3.149±0.242	2.875±0.224	2.703±0.314	DDD	2.913	2.643	2.633	2.623		2.640	2,5,6
80686	4.110±0.270	3.646±0.226	3.661±0.284	DDD							
89937	2.588±0.260	2.372±0.188	2.216±0.252	DCD	2.510	2.200	2.179	2.160			2,5
93017	3.847±0.254	3.611±0.252	3.655±0.042	DDE							
99825	4.112±0.294	3.582±0.266	3.501±0.232	DDD	4.160	3.740	3.670	3.600			2,5
102485	3.363±0.258	3.104±0.184	3.094±0.262	DCD							
105858	3.340±0.248	2.992±0.224	2.969±0.252	DDD	3.276	2.988	2.920	2.882	2.890	2.923	2,3
109176	2.954±0.222	2.729±0.184	2.564±0.290	DCD							
113283	4.533±0.037	3.804±0.210	3.805±0.240	ECD	4.480	3.940	3.830	3.790			2,5
116771	3.299±0.286	2.988±0.240	2.946±0.288	DDD			2.825				2
FGK stars (15 pc $< d \leq$ 20 pc)											
5862	4.094±0.346	3.719±0.268	3.782±0.268	DDD	3.980	3.712	3.666	3.635			2,5
17651	3.609±0.302	3.393±0.236	3.353±0.270	DDD							
36366	3.221±0.232	3.156±0.246	2.978±0.316	DDD	3.517		3.329	3.325	3.270		2,6,8
44248	3.209±0.268	3.082±0.254	3.003±0.358	DDD			2.880				2
46509	3.907±0.252	3.582±0.210	3.560±0.242	DCD	3.750	3.540	3.500	3.490			2,5
48113	3.961±0.318	3.725±0.262	3.609±0.017	DDE	4.040	3.710	3.670				2,5
61174	3.609±0.250	3.372±0.240	3.372±0.302	DDD	3.690	3.570	3.540	3.510	3.550	3.590	2
64241	3.399±0.244	3.266±0.218	3.108±0.246	DDD			3.200				
67153	3.585±0.268	3.347±0.220	3.410±0.248	DDD							
71284	3.561±0.250	3.462±0.246	3.336±0.324	DDD	3.705	3.514	3.490	3.487	3.480	3.465	2,5,6,7,8,9,10
75312	4.052±0.226	3.701±0.236	3.714±0.216	DDC							
77760	2.940±0.174	2.744±0.164	2.583±0.202	CCC	3.490	3.152	3.119	3.094	3.070		2,4,5,6,7
88745	3.459±0.198	3.242±0.190	3.107±0.230	CCD	3.660	3.500	3.550				2
104858	3.736±0.260	3.410±0.216	3.384±0.252	DCD							
112447	3.358±0.254	3.078±0.214	2.961±0.286	DCD	3.239		2.926	2.923	2.860		2,6,8

Note: We name HIP 7751A=HD 10360, HIP 7751B=HD 10361.

2MASS JHK_s are from the 2MASS Point Source Catalogue (II/246 in Vizier). Zero points for calibration from magnitudes to fluxes are from Cohen et al. (2003).

References for the $JHKLL'M$ photometry:
1. Carter (1990), SAAO infrared standards: http://www.saao.ac.za/fileadmin/files/links/IRstd.txt
2. Gezari et al. (2000), http://ircatalog.gsfc.nasa.gov/, also at Vizier, Catalogue no. II/225. (only magnitudes flagged 'M')
3. Koornneef (1983)
4. CVF standards http://www.iac.es/telescopes/pages/es/inicio/utilidades.php#CVF
5. Aumann & Probst (1991)
6. UKIRT very bright standards http://www.jach.hawaii.edu/UKIRT/astronomy/calib/phot_cal/bright_stds.html
7. Selby et al. (1988)
8. Glass (1975)
9. Old, bright, UKIRT standards http://www.jach.hawaii.edu/UKIRT/astronomy/calib/phot_cal/ukirt_stds.html
10. Elias et al. (1982)

Table 5c. AKARI 9 and 18 μm fluxes and WISE W1, W3 and W4 photometry.

HIP	AKARI		WISE		
	9 μm (mJy)	18 μm (mJy)	3.35 μm (W1) (mag)	11.56 μm (W3) (mag)	22.09 μm (W4) (mag)
FGK stars ($d \leq 15$ pc)					
1599	4193±28	1055±30		2.856±0.011	2.788±0.019
3765	2199±15	519±8		3.370±0.039	3.493±0.023
7751	3431±198	892±20			3.095±0.053
7751B	1810±135				
7918	2280±24	494±12	3.489±0.423	3.469±0.012	3.444±0.018
7981	2724±5	586±39	3.274±0.479		3.312±0.033
10644	2890±17	668±39		3.187±0.012	3.221±0.024
12114	2506±19	486±20		3.273±0.020	3.383±0.019
12843	2618±9	623±83		3.336±0.010	3.243±0.019
14879	5683±13	1346±11	2.653±0.163	2.360±0.004	2.440±0.015
15457	2789±21	619±45	3.263±0.461	3.277±0.010	3.240±0.020
15510	5692±25	1271±21			
16852	3903±5	850±21		2.905±0.015	2.868±0.021
22449	8357±36	1876±61		2.136±0.012	2.090±0.018
23693	2402±6	583±14	3.425±0.488	3.424±0.011	3.336±0.019
27072	6176±34		3.085±0.017	2.261±0.006	2.394±0.014
37279	109400±1730	22930±197		–0.425±0.427	–0.637±0.005
47080	2004±26	483±14		3.642±0.013	3.608±0.021
56997	2044±15	434±31	3.572±0.397	3.743±0.053	3.584±0.031
57443	2857±14	624±9		3.302±0.013	3.241±0.025
57757	6914±6	1558±23		2.386±0.013	2.294±0.016
59199	3027±10	707±35		3.189±0.013	3.113±0.017
61317	4325±20	993±23		2.733±0.026	2.764±0.020
61941	10480±138	2225±43		1.971±0.012	1.858±0.015
64394	3975±30	900±20		2.858±0.013	2.827±0.017
64924	3380±34	838±42		3.091±0.009	2.986±0.019
70497	4156±19	993±19	3.149±0.058	2.606±0.004	2.777±0.013
72659	5454±26	1233±53	2.788±0.310	2.887±0.026	2.831±0.024
73695	3370±41	790±35		3.060±0.009	3.049±0.017
77257	3590±37	776±10		3.000±0.011	2.971±0.020
78072	4911±18	1064±34		2.677±0.007	2.628±0.018
80686	2155±18	513±25	3.582±0.317	3.536±0.013	3.511±0.021
89937	7653±17	1701±15		2.252±0.014	2.154±0.016
93017	1896±6	432±35	3.708±0.386	3.679±0.014	3.641±0.019
99825		448±5	3.684±0.505	3.587±0.024	3.645±0.022
102485	3252±17	775±26		3.145±0.014	3.104±0.021
105858	3845±27	912±15	3.706±0.244	4.239±0.013	2.761±0.016
109176	5028±18	1184±40		2.671±0.007	2.619±0.020
113283	1716±9		3.897±0.411	3.698±0.010	3.770±0.021
116771	4124±59	863±15		2.911±0.013	2.859±0.021
FGK stars (15 pc < $d \leq 20$ pc)					
5862	1940±9	377±4		3.652±0.013	3.613±0.025
17651	3003±37	719±34	3.209±0.530	3.173±0.009	3.134±0.022
36366	2767±30	559±23	3.353±0.389	3.322±0.009	3.233±0.020
44248	3965±43	904±43		2.904±0.015	2.839±0.018
46509		550±25		3.521±0.012	3.457±0.020
48113	1930±14	458±36	3.621±0.377	3.656±0.015	3.619±0.022
61174	2631±15	837±6		3.308±0.016	2.752±0.023
64241	2976±9	696±25		3.219±0.012	3.165±0.024
67153	2645±13	657±30		3.344±0.012	3.272±0.019
71284	2226±19	519±31	3.478±0.415	3.507±0.010	3.444±0.019
75312	1960±9	465±24	3.649±0.503	3.651±0.015	3.608±0.021
77760	3202±10	717±21		3.115±0.010	3.073±0.019
88745	2085±17	520±22	3.587±0.358	3.578±0.015	3.552±0.022
104858	2791±32	658±7		3.290±0.013	3.247±0.026
112447	3970±36	925±32		2.910±0.013	2.884±0.021

Notes: We name HIP 7751B=HD 10361.

AKARI 9 and 18 μm fluxes and uncertainties are from the AKARI/IRC mid-IR all-sky Survey (ISAS/JAXA, 2010, catalogue II/297 in Vizier).

WISE data are from the AllWISE Data Release (Cutri et al. 2013), Vizier catalogue II/328, except for HIP 14879, HIP 27072, HIP 70497 and HIP 72659 that are from the WISE All-Sky Data Release (Cutri et al. 2012, Vizier catalogue II/311/wise). Zero points for calibration are from Wright et al. (2010).

Table 5d. IRAS 12, 25, 60 μm and *Spitzer*/MIPS 24 and 70 μm fluxes.

HIP	IRAS						MIPS	
	12 μm (mJy)	%	25 μm (mJy)	%	60 μm (mJy)	%	24 μm (mJy)	70 μm (mJy)
FGK stars ($d \leq 15$ pc)								
1599	3.11×10^3	4	6.95×10^2	4			519±11	82 ±8
3765	1.56×10^3	7					264±5	26 ±10
7751	2.70×10^3	5	6.55×10^2	7			231±5	22 ±4
7918	1.67×10^3	5	3.87×10^2	8			289±6	25 ±11
7981	1.87×10^3	7	6.38×10^2	10			334±7	48 ±9
10644	2.11×10^3	5	4.97×10^2	6			359±7	43 ±5
12114	1.83×10^3	5	3.47×10^2	14			311±6	35 ±6
12843	1.93×10^3	6					346±7	37 ±13
14879	4.02×10^3	4	9.43×10^2	4	1.80×10^2	18	754±15	105 ±13
15457	2.05×10^3	4	4.67×10^2	8			340±7	39 ±8
15510	4.27×10^3	4	9.50×10^2	5	1.89×10^2	17	722±15	100 ±8
16852	2.85×10^3	5	6.81×10^2	8			502±10	106 ±9
22449	5.67×10^3	12	1.51×10^3	7	2.04×10^2	20	1020±21	116 ±9
23693	1.67×10^3	5	4.40×10^2	8			308±6	6 ±7
27072	4.40×10^3	5	9.81×10^2	6	2.28×10^2	16	765±16	56 ±10
37279	8.29×10^4	4	1.87×10^4	5	3.00×10^3	6		1520 ±103
47080	1.47×10^3	5	3.49×10^2	11			257±5	581 ±0
56997							258±5	30 ±5
57443	2.03×10^3	7	4.92×10^2	10			334±7	32 ±6
57757	5.24×10^3	7	1.21×10^3	10	1.79×10^2	25	829±17	114 ±1
59199	2.45×10^3	7	5.52×10^2	9			368±8	46 ±6
61317	3.49×10^3	5	7.29×10^2	6			557±11	65 ±1
61941	7.67×10^3	6	1.70×10^3	7	2.91×10^2	20	1410±29	238 ±122
64394	2.98×10^3	7	6.46×10^2	8			489±10	49 ±6
64924	2.56×10^3	6	5.80×10^2	12			443±9	192 ±16
70497	3.08×10^3	4	7.24×10^2	5	1.09×10^2	28	540±11	63 ±8
72659	3.90×10^3	5	8.95×10^2	6	1.57×10^2	25	476±10	53 ±7
73695	2.50×10^3	4	5.88×10^2	5			468±10	70 ±12
77257	2.46×10^3	4	5.91×10^2	7			433±9	84 ±15
78072	3.82×10^3	5	8.82×10^2	5	3.32×10^2	12	630±13	70 ±17
80686	1.58×10^3	4	3.68×10^2	6			284±6	21 ±13
89937	5.51×10^3	3	1.31×10^3	4	2.20×10^2	14	1050±21	127 ±10
93017	1.44×10^3	4	3.47×10^2	6			239±5	25 ±6
99825	1.49×10^3	6	4.04×10^2	23			237±5	22 ±4
102485	2.35×10^3	7	5.14×10^2	14			391±8	44 ±8
105858	2.95×10^3	4	6.42×10^2	6	1.72×10^2	21	472±10	44 ±6
109176	3.70×10^3	7	8.55×10^2	11			667±14	75 ±7
113283	1.27×10^3	6	3.45×10^2	13			213±4	27 ±4
116771	2.97×10^3	6	7.37×10^2	15			511±10	61 ±8
FGK stars (15 pc $< d \leq 20$ pc)								
5862	1.44×10^3	7	3.45×10^2	14			246±5	45 ±5
17651	2.19×10^3	5	4.76×10^2	7			366±8	48 ±5
36366	2.01×10^3	5	4.82×10^2	21			356±7	42 ±7
44248	2.94×10^3	5	7.41×10^2	7			518±11	
46509	1.69×10^3	5	3.37×10^2	14			258±5	31 ±4
48113	1.48×10^3	5	3.27×10^2	9			247±5	33 ±5
61174	2.24×10^3	6	7.70×10^2	8	3.08×10^2	14	573±12	20 ±14
64241	2.19×10^3	6	5.11×10^2	13			385±8	50 ±11
67153	1.93×10^3	5	4.22×10^2	10			332±7	106 ±76
71284	1.61×10^3	5	4.13×10^2	7	1.40×10^2	25	302±6	72 ±11
75312	1.43×10^3	5	3.41×10^2	9			273±6	70 ±12
77760	2.31×10^3	5	5.71×10^2	6			402±8	40 ±6
88745	1.52×10^3	5	3.50×10^2	8			268±6	107 ±9
104858	2.21×10^3	7	5.42×10^2	8			362±7	43 ±5
112447	3.05×10^3	7	7.56×10^2	9			467±10	50 ±5

Notes: All IRAS fluxes are from the Faint Source Catalogue (II/156A in Vizier) except for HIP 3765 which are from the IRAS Catalogue of Point Sources (II/125). Upper limits to the fluxes are not given.

Spitzer/MIPS fluxes at 24 and 70 μm were extracted by members of the DUNES team. See http://sdc.cab.inta-csic.es/dunes/HELP/DUNES_Archive_ReadMe.jsp or http://sdc.cab.inta-csic.es/dunes/HELP/DUNES_Archive_ReadMe.pdf for details.

Table 6. OBSIDs for the DUNES_DB stars with $d \leq 20$ pc.

HIP	HD	PACS	Scan	X-Scan	On-source time [s]
FGK stars ($d < 15$ pc)					
1599	1581	100/160	1342198529	1342198530	288
3765	4628	100/160	1342213215	1342213216	288
7751	10360	100/160	1342193169	1342193170	288
	10361	100/160	1342193169	1342193170	288
7918	10307	100/160	1342223568	1342223569	288
7981	10476	100/160	1342213522	1342213523	288
10644	13974	100/160	1342223878	1342223879	288
12114	16160	100/160	1342215727	1342215728	288
12843	17206	100/160	1342214006	1342214007	288
14879	20010	100/160	1342202298	1342202299	288
15457	20630	100/160	1342216133	1342216134	288
15510	20794	100/160	1342216456	1342216457	1080
16852	22484	100/160	1342224212	1342224213	288
22449	30652	100/160	1342193142	1342193143	288
23693	33262	100/160	1342205208	1342205209	288
27072	38393	100/160	1342203715	1342203716	288
37279	61421	100/160	1342208989	1342208990	1080
47080	82885	100/160	1342209372	1342209373	288
56997	101501	100/160	1342211430	1342211431	288
57443	102365	100/160	1342202240	1342202241	288
57757	102870	100/160	1342212383	1342212384	288
59199	105452	100/160	1342212824	1342212825	288
61317	109358	100/160	1342208821	1342208822	288
61941	110379J	100/160	1342212644	1342212645	288
64394	114710	100/160	1342212672	1342212672	288
64924	115617	100/160	1342202551	1342202552	288
70497	126660	100/160	1342209638	1342209639	288
72659	131156	100/160	1342213800	1342213801	288
73695	133640	100/160	1342208966	1342208967	288
77257	141004	100/160	1342204158	1342204159	288
78072	142860	100/160	1342215378	1342215379	288
80686	147584	100/160	1342216577	1342216578	288
89937	170153	100/160	1342220810	1342220811	288
93017	176051	100/160	1342205038	1342205039	288
99825	192310	100/160	1342208466	1342208467	288
102485	197692	100/160	1342193530	1342193531	288
105858	203608	100/160	1342215352	1342215353	288
109176	210027	100/160	1342198503	1342198504	288
113283	216803	100/160	1342211140	1342211141	288
116771	222368	100/160	1342198507	1342198508	288
FGK stars (15 pc < $d \leq$ 20 pc)					
5862	7570	100/160	1342213175	1342213176	288
17651	23754	100/160	1342223596	1342223596	288
36366	58946	100/160	1342219410	1342219411	288
44248	76943	100/160	1342208506	1342208507	288
46509	81997	100/160	1342209475	1342209476	288
48113	84737	100/160	1342210446	1342210447	288
61174	109085	100/160	1342234385	1342234386	288
64241	114378J	100/160	1342212720	1342212721	288
67153	119756	100/160	1342203109	1342203110	288
71284	128167	100/160	1342213660	1342213661	288
75312	137107J	100/160	1342213788	1342213789	288
77760	142373	100/160	1342205167	1342205168	288
88745	165908	100/160	1342195362	1342195363	288
104858	202275	100/160	1342195606	1342195607	288
112447	215648	100/160	1342198505	1342198506	288

Table 7. PACS flux densities for the DUNES_DB stars with $d \leq 15$ pc and $15\,\mathrm{pc} < d \leq 20$ pc.

HIP	HD	PACS100 (mJy)	S100 (mJy)	χ_{100}	PACS160 (mJy)	S160 (mJy)	χ_{160}	Status
FGK stars ($d \leq 15$ pc)								
1599	1581	33.23± 2.35	30.08± 0.19	1.34	29.03±3.46	11.75± 0.07	4.99	Dubious
3765	4628	19.43± 1.93	15.84± 0.36	1.83	< 3.38	6.19± 0.14		No excess
7751	10360	11.95± 1.70	12.39± 0.21	−0.26	< 5.00	4.84± 0.08		No excess
	10361	10.66± 1.68	14.90± 0.26	−2.49	< 5.00	5.82± 0.10		No excess
7918	10307	14.33± 1.75	16.21± 0.25	−1.06	10.35±3.17	6.33± 0.10	1.27	No excess
7981	10476	20.18± 1.91	20.05± 0.21	0.07	7.87±2.05	7.83± 0.08	0.02	No excess
10644	13974	23.45± 2.07	20.75± 0.30	1.29	6.59±3.60	8.11± 0.12	−0.42	No excess
12114	16160	15.29± 1.74	17.26± 0.24	−1.12	5.91±3.32	6.74± 0.09	−0.25	No excess
12843	17206	20.94± 2.08	19.10± 0.22	0.88	7.52±3.18	7.46± 0.09	0.02	No excess
14879	20010	40.72± 2.70	38.77± 1.48	0.63	24.90±3.58	15.14± 0.58	2.69	No excess
15457	20630	24.78± 2.02	19.85± 0.24	2.43	12.14±2.52	7.75± 0.09	1.74	No excess
15510 *	20794	48.62± 2.64	40.60± 0.34	3.01	27.12±2.33	15.86± 0.13	4.82	Excess
16852 *	22484	67.30± 3.64	28.09± 0.34	10.71	33.35±3.19	10.97± 0.13	7.01	Excess
22449	30652	65.99± 3.67	58.79± 0.29	1.95		22.97± 0.12		No excess
23693	33262	33.97± 2.33	17.49± 0.42	6.97	9.39±2.84	6.83± 0.17	0.90	Excess
27072	38393	49.21± 2.95	43.99± 0.29	1.76	19.67±3.13	17.18± 0.11	0.80	No excess
37279	61421	867.50±43.38	733.50± 8.48	3.03	355.75±17.88	286.50± 3.31	3.81	Dubious
47080	82885	10.12± 1.87	13.56± 0.21	−1.83	8.30±3.16	5.30± 0.08	0.94	No excess
56997	101501	15.43± 1.71	14.83± 0.14	0.35	12.69± 3.51	5.79± 0.05	1.97	No excess
57443	102365	16.22± 1.96	19.83± 0.17	−1.84	< 3.85	7.74± 0.07		No excess
57757	102870	68.43± 3.80	48.38± 0.23	5.26	40.67±3.83	18.90± 0.09	5.68	Excess
59199	105452	27.10± 2.16	21.65± 0.34	2.49	25.40±3.29	8.46± 0.13	5.14	Dubious
61317	109358	31.43± 2.34	30.76± 0.30	0.28	9.52±3.46	12.02± 0.12	−0.72	No excess
61941	110379J	85.77± 4.59	71.92± 0.86	2.97	49.43±3.86	28.10± 0.34	5.50	Dubious
64394	114710	23.74± 1.98	28.55± 0.25	−2.41	13.50±3.26	11.15± 0.10	0.72	No excess
64924 *	115617	211.56±10.74	23.67± 1.10	17.40	161.27±8.74	9.24± 0.43	17.37	Excess
70497	126660	36.36± 2.46	30.16± 0.33	2.50	15.57±3.17	11.78± 0.13	1.20	No excess
72659	131156	57.51± 7.46	27.42± 0.55	4.02	42.14±8.58	10.71± 0.21	3.66	Dubious
73695	133640	32.17± 2.15	24.01± 0.25	3.77	30.83±2.94	9.38± 0.10	7.30	Dubious
77257	141004	33.11± 2.35	25.19± 0.42	3.32	20.23±3.12	9.84± 0.16	3.33	Dubious
78072	142860	30.71± 2.26	35.81± 0.20	−2.25	24.40±3.91	13.99± 0.08	2.66	No excess
80686	147584	17.31± 1.75	15.45± 0.28	1.05	< 3.92	6.03± 0.11		No excess
89937	170153	57.97± 3.27	55.98± 0.31	0.61	32.41±3.72	21.87± 0.12	2.83	No excess
93017	176051	18.73± 1.79	13.38± 0.26	2.95	< 5.02	5.23± 0.10		No excess
99825	192310	11.79± 1.87	14.17± 0.16	−1.27	8.32±3.35	5.53± 0.06	0.83	No excess
102485	197692	27.11± 2.35	23.05± 0.20	1.72	9.13±3.09	9.00± 0.08	0.04	No excess
105858	203608	30.87± 2.23	28.59± 0.46	1.00	14.85±3.34	11.17± 0.18	1.10	No excess
109176	210027	34.70± 2.38	34.35± 0.51	0.14	16.90±3.39	13.42± 0.20	1.03	No excess
113283	216803	12.21± 1.57	12.48± 0.25	−0.17	12.69±1.73	4.87± 0.10	4.51	Excess
116771	222368	42.11± 2.66	29.19± 0.44	4.79	21.75±3.33	11.40± 0.17	3.10	Excess
FGK stars ($15\,\mathrm{pc} < d \leq 20$ pc)								
5862	7570	24.36±2.03	13.83± 0.14	5.16	7.33±3.29	5.40± 0.06	0.59	Excess
17651	23754	26.70±2.16	21.10± 0.53	2.52	8.22±3.23	8.24± 0.21	−0.01	No excess
36366	58946	22.24±1.92	18.79± 0.32	1.77	18.78±3.47	7.34± 0.12	3.30	Dubious
44248	76943	34.66±2.29	28.35± 0.59	2.67	22.61±3.38	11.07± 0.23	3.40	Dubious
46509	81997	19.15±1.91	16.06± 0.13	1.62	9.20±3.36	6.27± 0.05	0.87	No excess
48113	84737	9.56±1.56	13.94± 0.14	−2.80	9.77±3.35	5.44± 0.06	1.29	No excess
61174 *	109085	252.00±16.00	16.00± 0.43	14.75	231.00±13.00	6.25± 0.17	17.29	Excess
64241	114378J	26.01±2.02	21.70± 0.14	2.13	16.09±3.09	8.48± 0.05	2.47	No excess
67153	119756	19.70±1.88	19.51± 0.20	0.10	5.72±2.84	7.62± 0.08	−0.67	No excess
71284	128167	39.45±2.57	16.13± 0.09	9.06	18.40±3.13	6.30± 0.04	3.87	Excess
75312	137107J	12.01±1.86	14.53± 0.25	−1.34	4.69±3.45	5.68± 0.10	−0.29	No excess
77760	142373	22.41±1.99	23.38± 0.16	−0.49	17.09±3.25	9.13± 0.06	2.45	No excess
88745 *	165908	87.00±10.00	15.69± 0.75	7.11	80.00±15.00	6.13± 0.29	4.92	Excess
104858	202275	25.12±2.00	20.14± 0.19	2.48	5.26±3.61	7.87± 0.07	−0.72	No excess
112447	215648	26.32±2.19	27.73± 0.29	−0.64	16.19±3.19	10.83± 0.11	1.68	No excess

Notes: * denotes that the source is extended.
The uncertainties $\sigma(\mathrm{PACS}_\nu(\lambda))$ for PACS100 and PACS160 are the statistical plus systematic, combined quadratically; values of 5% of the fluxes for the systematic –calibration– uncertainties were considered at both wavelengths (Balog et al. 2014).

PACS fluxes for HIP 61174 are from Duchêne et al. (2014).
PACS fluxes for HIP 88745 are from Kennedy et al. (2012).
HIP 7751 has been treated as a single source in the statistical analysis of the sample.
HIP 72659 is a binary (G7-8V+K5V) however the SED is bets fitted with the G8 photosphere only.
HIP 73695 is a W UMa eclipsing binary (F5V+G9V), however the SED is best fitted with the G9 photosphere only.
S100 and S160 values for HIP 88745 (F7V+K4V) are from a composite model to include both components of the binary.

PACS70 fluxes for HIP 15510 (100.0±5.0 mJy, Kennedy et al. 2012), HIP 61174 (230.0±13.0 mJy, Duchêne et al. 2014), HIP 64924 (198.0±3.0 mJy, Wyatt et al. 2012) and HIP 88745 (93.0±10.0 mJy, Kennedy et al. 2012) have been also used in this work.

In addition to the PACS data, SPIRE flux densities have been included in the SEDs of these sources:
HIP 61174: 100.0±10.0 (250 μm), <100.0 (350 μm), <10.0 mJy (500 μm) (Duchêne et al. 2014).
HIP 64294: 129.0±21.0 (250 μm), 55.0±17.0 (350 μm), 20.0±12.0 mJy (500 μm) (Wyatt et al. 2012).
HIP 88745: 44.0±6.0 (250 μm), 22.0±7.0 (350 μm) (Kennedy et al. 2012).